

Characteristics and Channel Capacity Studies of a Novel 6G Non-Stationary Massive MIMO Channel Model Considering Mutual Coupling

Yue Yang, Cheng-Xiang Wang, *Fellow, IEEE*, Jie Huang, *Member, IEEE*,
John Thompson, *Fellow, IEEE*

Abstract

In the sixth generation (6G) wireless communication networks, ultra-massive multiple-input multiple-output (MIMO) communication is one of the most promising technologies. In ultra-massive MIMO channels, the mutual coupling (MC) effect is more obvious when antenna elements are more closely spaced. In this paper, a novel 6G space-time-frequency (STF) non-stationary massive MIMO channel model is proposed, which jointly considers MC, antenna efficiency, and near-field steering vectors of different antenna topologies. As the Shannon capacity theorem is based on the wide-sense stationary (WSS) channel assumption and cannot be applied to non-stationary channels, we propose a novel non-stationary channel capacity calculation method that divides the non-stationary channel into WSS sub-channels. Important statistical properties and channel capacities of the proposed channel model are derived and verified by ultra-massive MIMO channel measurements and data post-processing. The results show that the simulated spatial cross-correlation function (CCF) and channel capacity considering MC and antenna efficiency are closer to measured results. It also shows that antenna topologies have an impact on channel capacities. Furthermore, channel capacities using the proposed novel calculation method match the measured channel capacities in non-stationary channels.

This work was supported by the National Natural Science Foundation of China (NSFC) under Grants 61960206006 and 62271147, the Fundamental Research Funds for the Central Universities under Grants 2242022k60006 and 2242023K5003, the Key Technologies R&D Program of Jiangsu (Prospective and Key Technologies for Industry) under Grants BE2022067 and BE2022067-1, the EU H2020 RISE TESTBED2 project under Grant 872172, the High Level Innovation and Entrepreneurial Doctor Introduction Program in Jiangsu under Grant JSSCBS20210082, and the Start-up Research Fund of Southeast University under Grant RF1028623029.

Y. Yang, C.-X. Wang (corresponding author), and J. Huang are with the National Mobile Communications Research Laboratory, School of Information Science and Engineering, Southeast University, Nanjing 210096, China, and also with the Purple Mountain Laboratories, Nanjing 211111, China (email: {yueyang, chxwang, j_huang}@seu.edu.cn).

J. Thompson is with the Institute for Digital Communications, School of Engineering, University of Edinburgh, Edinburgh EH9 3JL, U.K. (email: john.thompson@ed.ac.uk).

Index Terms

6G massive MIMO channel model, space-time-frequency non-stationarity, mutual coupling, near-field steering vectors, non-stationary channel capacity.

I. INTRODUCTION

Wireless communications aim to continuously improve the coverage and achieve high transmission data rate [1]. In wireless communication systems, the electromagnetic theory and information theory are two cornerstones, which can be connected by the wireless channel modeling theory and antenna theory. The integration of electromagnetic theory and information theory is called electromagnetic information theory, which attracts more attention from researchers recently [2]–[5]. The electromagnetic theory can reflect physical phenomena in communication systems and the information theory can characterize system performances in a mathematical manner [6], [7]. [The wireless propagation channel links the transmitter \(Tx\) and receiver \(Rx\) antennas and carries information via electromagnetic waves, acting as the bridge connecting electromagnetic theory and information theory. The wireless channel modeling theory is of great importance for channel estimation, channel capacity analysis, and network planning.](#) However, the influences of new channel characteristics on system performance are not clear, such as space-time-frequency (STF) non-stationarities and near-field effects in ultra-massive multiple-input multiple-output (MIMO). To propose a physically consistent channel model that can characterize communication environments, it is essential to use the electromagnetic information theory to model and analyze the wireless channels.

In the sixth generation (6G) wireless communications, ultra-massive MIMO evolving from massive MIMO with hundreds of antenna elements, shows an excellent performance in high spectral efficiency, high energy efficiency, and robustness [8], [9]. In [10]–[12], the cluster evolution on time and array axes and spherical wavefront (SWF) in massive MIMO channel models were modeled, validating 6G channels can exhibit non-stationarities in STF domains since multi-antenna, high mobility, and large bandwidth at high-frequency bands, respectively. When the number of antennas increases, the distance between the Tx and Rx may be sufficiently small that the plane wavefront (PWF) assumption may not be fulfilled. In [13], a non-stationary massive MIMO channel model was proposed and the statistical properties in the space domain and channel capacities of non-stationary channels were studied. Remarkably, compared to deterministic channel models [14]–[16], geometry-based stochastic models (GBSMs) [17]–[19] are

more accurate and flexible, and often used for system simulations in 6G wireless communication systems.

As the antenna element number increases and antenna spacing decreases in ultra-massive MIMO, there is always a portion of the energy from the antenna coupled to the other antennas, which is the mutual coupling (MC) effect [20]. This physical phenomenon will be more prominent in 6G ultra-massive MIMO and holographic MIMO channels [21]. In [22], MC was obtained with the dipoles displacing in different antenna topologies, which can impact the mutual impedance. In [23] and [24], a multi-port circuit model and an equivalent antenna circuit were used to characterize the communication systems. In [25] and [26], the authors analyzed the influence of MC on channel capacity by different methods. In [27], the achievable rate of a wideband channel with a compact antenna array was analyzed, and optimal antenna spacing considering MC was studied. [This work also claimed that the performance degradation due to MC effect can be declined by adopting a proper matching method for wideband antennas and can achieve the maximum achievable rate.](#) In [28], the influence of MC on antenna pattern and antenna efficiency in MIMO systems was illustrated. Furthermore, the steering vectors represent the spatial phase difference caused by the electromagnetic waves coming from a certain direction, which are important for beamforming and positioning [29], [30]. The steering vector of a uniform linear array (ULA) in the far field was used in [31], which needs to be expanded to other antenna topologies and for use in the near field. The boundary between near-field and far-field is the Rayleigh distance. It is calculated as $2L^2/\lambda$, where L and λ are antenna aperture and wavelength, respectively. In [32], the authors analyzed the impacts of antenna elements and spacing on antenna gain in massive MIMO systems with ULA and uniform circular array (UCA). In [33], the spectral efficiency of massive MIMO channels with ULA, uniform plane array (UPA), and UCA in the far field were analyzed. In short, most MIMO channel models did not jointly consider the influences of radiation efficiency, MC, and near-field steering vectors of different antenna topologies on system performance.

The channel capacity is one of the key performance indicators in wireless communications. Telatar gave the channel capacity formulas in different knowledge of channel state information (CSI) at the Tx and Rx for the first time in [34]. Channel capacities of multi-antenna channel models with spatial correlation and MIMO channels with intelligent reflecting surface were analyzed in [35] and [36], respectively. In [37], the authors proposed a three-dimensional (3D) non-stationary GBSM with visibility region and calculated the channel capacity. In [38], the

spatio-temporal water-filling algorithm was used to determine the channel capacity when the Tx and Rx know the CSI. However, the traditional Shannon channel capacity is based on the wide-sense stationary (WSS) channel assumption, which is not applicable in non-stationary channels. A channel capacity calculation method for non-stationary channel models needs to be studied in STF non-stationary channels.

Currently, the massive MIMO channel models have only considered the STF non-stationarity, MC, and far-field antenna steering vectors separately, and the influences of these factors on channel capacity are not sufficiently investigated and verified. In addition, the capacity calculation method can only be used in WSS channels. [This paper further extends our previous work in \[13\] to fill the research gaps. Specifically, \[13\] only considered the MC effect in a non-stationary massive MIMO channel model and analyzed the spatial cross-correlation function \(CCF\) as well as channel capacities. In this paper, the proposed novel 6G STF non-stationary massive MIMO channel model jointly considers antenna MC effect, antenna efficiency, and near-field steering vectors.](#) The cluster evolution on time, array, and frequency axes is introduced, and a novel channel capacity calculation method is proposed. The main contributions and novelties of this paper are summarized as follows.

- 1) A novel 6G STF non-stationary massive MIMO channel model considering antenna MC effect, antenna efficiency, and near-field steering vectors of different antenna topologies is proposed. The electromagnetic theory and antenna theory are used to characterize the MC effect and antenna efficiency. The proposed channel model also contains the near-field steering vectors of ULA, UPA, and UCA.

- 2) A novel non-stationary channel capacity calculation method using the stationary intervals (SIs) in the STF domains is proposed. Non-stationary channel capacities are the summation of the segmented WSS sub-channel capacities.

- 3) Important statistical properties in the STF domains and non-stationary channel capacities are derived and verified by 6G ultra-massive MIMO channel measurements.

The remainder of this paper is organized as follows. In Section II, a 6G STF non-stationary massive MIMO channel model is established. Statistical properties and non-stationary channel capacities are derived in Section III. Analytical and simulation results verified by channel measurements are presented in Section IV. Finally, Section V draws the conclusions.

II. A 6G STF NON-STATIONARY MASSIVE MIMO CHANNEL MODEL

A 6G STF non-stationary massive MIMO channel model is proposed in this section, which jointly considers the MC, antenna efficiency, and near-field steering vectors. The channel fading includes large-scale fading (LSF) and small-scale fading (SSF). The LSF includes path loss and shadow fading caused by obstacles, such as buildings, mountains, and trees. The SSF is caused by multipath propagation, which is shown in the characteristics of clusters and rays.

A. Channel Matrix

The channel matrix is the multiplication of the LSF and SSF, which can be expressed as

$$\mathbf{H} = \sqrt{PL \cdot SF \cdot BP \cdot AL \cdot BL} \cdot \mathbf{C}_r \cdot \mathbf{H}_{\text{SSF}} \cdot \mathbf{C}_t^H \quad (1)$$

where PL is path loss, SF is shadow fading, BP is building penetration loss, AL is atmosphere absorption loss, and BL is blockage loss. The SSF matrix is denoted as \mathbf{H}_{SSF} and it contains the channel impulse response (CIR) of the p th Tx antenna and q th Rx antenna at carrier frequency f_c , where $p = 1, \dots, N_t$, $q = 1, \dots, N_r$. The SSF can be written as $\mathbf{H}_{\text{SSF}} = [h_{qp,f_c}(t, \tau)]_{N_r \times N_t}$, where N_t and N_r are the numbers of Tx and Rx antennas, respectively. The MC matrices at Tx and Rx denote as \mathbf{C}_t and \mathbf{C}_r , respectively. The operator $\{\cdot\}^H$ is the conjugate transposition.

The real channel environments can be classified into rural macro, urban macro, urban micro scenarios, etc. The path loss indicates the power loss during the signal transmission along paths, which is related to the propagation distance and frequency [39]. When the channel is in higher frequency band and has larger bandwidth, the building penetration and atmosphere loss are much more obvious, especially in millimeter wave (mmWave) and terahertz (THz) channels. The blockage losses accounting for phase shifts in the diffraction model verified by measurements were shown in [40] and [41].

The proposed 6G STF non-stationary massive MIMO channel model is illustrated in Fig. 1. This channel model is built in the Cartesian coordinate system, and the clusters are represented as spheres and the rays in the clusters are small blue dots in the sphere. The m th ray in the n th cluster is denoted as $r_{n,m}$, where $m = 1, 2, \dots, M(t)$ and $n = 1, 2, \dots, N(t)$. The dashed line between different clusters means a virtual link. Key parameters of the proposed channel model are listed in Table I. The CIR of this proposed channel model can be expressed as [18]

$$h_{qp,f_c}(t, \tau) = \sqrt{\frac{K_R(t)}{K_R(t) + 1}} h_{qp,f_c}^{\text{LoS}}(t, \tau) + \sqrt{\frac{1}{K_R(t) + 1}} h_{qp,f_c}^{\text{NLoS}}(t, \tau) \quad (2)$$

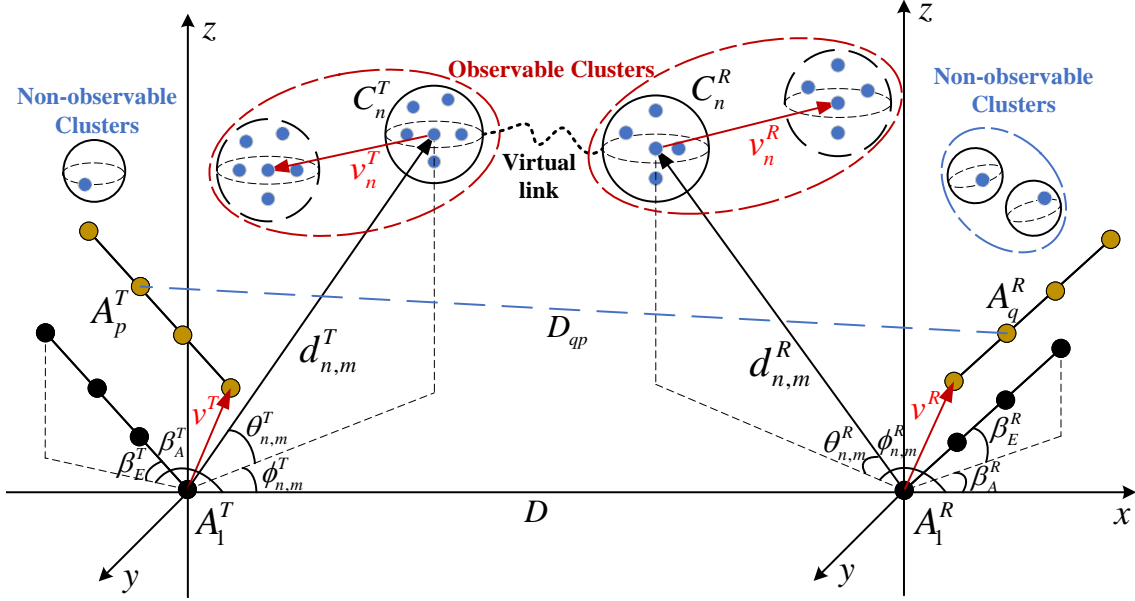


Fig. 1. A 6G STF non-stationary massive MIMO channel model.

where $h_{qp,f_c}^{\text{LoS}}(t, \tau)$ is the CIR of line-of-sight (LoS) component and $h_{qp,f_c}^{\text{NLoS}}(t, \tau)$ is the CIR of non-LoS (NLoS) component. The variable $K_R(t)$ is the time-variant Rician K-factor, which measures the ratio of LoS power to NLoS power. The CIR of the LoS component is

$$\begin{aligned}
 h_{qp,f_c}^{\text{LoS}}(t, \tau) = & \begin{bmatrix} F_{q,H}(\theta_L^R, \phi_L^R) \\ F_{q,V}(\theta_L^R, \phi_L^R) \end{bmatrix}^T \begin{bmatrix} e^{j\Phi_L^{\theta\theta}} & 0 \\ 0 & e^{j\Phi_L^{\phi\phi}} \end{bmatrix} \begin{bmatrix} F_{p,H}(\theta_L^T, \phi_L^T) \\ F_{p,V}(\theta_L^T, \phi_L^T) \end{bmatrix} \cdot \left(\frac{f}{f_c}\right)^{\gamma_L} \\
 & \cdot e^{-j\frac{2\pi}{\lambda}d_{2D}} \cdot e^{j2\pi f_c \tau_{qp}^L(t)} \cdot \delta(\tau - \tau_{qp}^L(t))
 \end{aligned} \quad (3)$$

where $\{\cdot\}^T$ is the transpose operator, θ_L^T and ϕ_L^T are elevation angle of departure (EAoD) and azimuth angle of departure (AAoD) of the LoS path, respectively, θ_L^R and ϕ_L^R are elevation angle of arrival (EAoA) and azimuth angle of arrival (AAoA) of the LoS path, respectively, $F_{q,H}$ and $F_{q,V}$ are the q th Rx antenna patterns in horizontal and vertical polarization directions, respectively. Similarly, $F_{p,H}$ and $F_{p,V}$ are the p th Tx antenna patterns in horizontal and vertical polarization directions, respectively [39]. In the LoS case, $\Phi_L^{\theta\theta}$ and $\Phi_L^{\phi\phi}$ are random initial phases with two combinations of polarization, which are uniform distributions within $[-\pi, \pi]$. The parameter γ_L is a scenario-dependent value in the LoS path, and it describes the trend of how amplitude decreases as frequency increases. The projection of the transceiver distance on the ground is denoted as d_{2D} . The propagation delay of the LoS path is

TABLE I
DEFINITIONS OF CHANNEL MODEL PARAMETERS.

Parameters	Definitions
A_p^T, A_q^R	The p th Tx antenna element and the q th Rx antenna element, respectively
δ_p, δ_q	Tx and Rx antenna spacings, respectively
C_n^T, C_n^R	The first bounce of the n th cluster at Tx and Rx, respectively
D_{qp}	Distance between the p th Tx and q th Rx
$N(t)$	The total number of clusters at time t
$M(t)$	The total number of rays in the n th cluster at time t
$\beta_E^{T(R)}, \beta_A^{T(R)}$	Elevation and azimuth angles of the Tx (Rx) antenna array, respectively
$v^T(t), v^R(t)$	Moving speeds of Tx and Rx array at time instant t , respectively
$v_n^T(t), v_n^R(t)$	Moving speeds of C_n^T and C_n^R at time instant t , respectively
$d_{n,m}^T, d_{n,m}^R$	Distances from A_1^T to C_n^T and from A_1^R to C_n^R via the m th ray at initial time, respectively
$d_{p,n,m}^T(t), d_{q,n,m}^R(t)$	Distances from A_p^T to C_n^T and from A_q^R to C_n^R via the m th ray at time t , respectively
$P_{qp,n,m}(t)$	Normalized power of the m th ray from the p th Tx antenna and q th Rx antenna at time t
$\tau_{qp,n,m}(t)$	Delay of the m th ray from the p th Tx antenna and q th Rx antenna at time t
$\theta_{n,m}^T, \phi_{n,m}^T$	EAoD and AAoD for the m th ray in n th cluster, respectively
$\theta_{n,m}^R, \phi_{n,m}^R$	EAoA and AAoA for the m th ray in n th cluster, respectively
α^T, α^R	Angles of moving Tx and Rx antenna array, respectively
$\theta_v^{T(R)}, \phi_v^{T(R)}$	Travel elevation and azimuth angles of Tx (Rx), respectively
$\theta_{v_n}^{T(R)}, \phi_{v_n}^{T(R)}$	Travel elevation and azimuth angles of C_n^T (C_n^R), respectively

$$\tau_{qp}^L(t) = D_{qp}(t)/c. \quad (4)$$

Here, $D_{qp}(t)$ is the relative distance of LoS path, which is calculated as [17]

$$D_{qp}(t) = \|\mathbf{l}_q^R - \mathbf{l}_p^T + \int_0^t \mathbf{v}^R(t) - \mathbf{v}^T(t)dt\| \quad (5)$$

where $\|\cdot\|$ denotes the Frobenius norm, \mathbf{l}_q^R is the distance vector between the q th and first Rx antenna element, and \mathbf{l}_p^T denotes the distance vector between the p th and first Tx antenna element, which can be expressed as [17]

$$\mathbf{l}_p^T = \delta_p \begin{bmatrix} \cos(\beta_E^T) \cos(\beta_A^T) \\ \cos(\beta_E^T) \sin(\beta_A^T) \\ \sin(\beta_E^T) \end{bmatrix}^T. \quad (6)$$

Time-variant velocity of Tx array is $\mathbf{v}^T(t)$, which is written as

$$\mathbf{v}^T(t) = v^T(t) \begin{bmatrix} \cos(\theta_v^T(t)) \cos(\phi_v^T(t)) \\ \cos(\theta_v^T(t)) \sin(\phi_v^T(t)) \\ \sin(\theta_v^T(t)) \end{bmatrix}^T. \quad (7)$$

When the Tx and Rx are traveling with constant velocity, $D_{qp}(t)$ in (5) can be calculated as

$$\begin{aligned} D_{qp}(t)^2 &= [\cos(\alpha^R)v^R t - \cos(\alpha^T)v^T t - \cos(\beta_E^T) \cos(\beta_A^T)\delta_p + \cos(\beta_E^R) \cos(\beta_A^R)\delta_q]^2 \\ &\quad + [\sin(\alpha^R)v^R t - \sin(\alpha^T)v^T t - \cos(\beta_E^T) \sin(\beta_A^T)\delta_p + \cos(\beta_E^R) \cos(\beta_A^R)\delta_q]^2 \\ &\quad + [\sin(\beta_E^T)\delta_p - \sin(\beta_E^R)\delta_q + \sin(\theta_v^R)v^R t - \sin(\theta_v^T)v^T t]^2 \end{aligned} \quad (8)$$

where $\cos(\alpha^R) = \cos(\theta_v^R) \cos(\phi_v^R)$ and $\sin(\alpha^R) = \cos(\theta_v^R) \sin(\phi_v^R)$, and the corresponding $\cos(\alpha^T)$ and $\sin(\alpha^T)$ can be obtained by substituting the superscript R with T .

The CIR of NLoS components can be written as

$$\begin{aligned} h_{qp,fc}^{\text{NLoS}}(t, \tau) &= \sum_{n=1}^{N(t)} \sum_{m=1}^{M(t)} \begin{bmatrix} F_{q,H}(\theta_{n,m}^R, \phi_{n,m}^R) \\ F_{q,V}(\theta_{n,m}^R, \phi_{n,m}^R) \end{bmatrix}^T \begin{bmatrix} e^{j\Phi_{n,m}^{\theta\theta}} & \frac{e^{j\Phi_{n,m}^{\theta\phi}}}{\sqrt{\kappa_{n,m}}} \\ \frac{e^{j\Phi_{n,m}^{\phi\theta}}}{\sqrt{\kappa_{n,m}}} & e^{j\Phi_{n,m}^{\phi\phi}} \end{bmatrix} \begin{bmatrix} F_{p,H}(\theta_{n,m}^T, \phi_{n,m}^T) \\ F_{p,V}(\theta_{n,m}^T, \phi_{n,m}^T) \end{bmatrix} \\ &\quad \sqrt{P_{qp,n,m}(t)} \cdot \left(\frac{f}{f_c}\right)^{\gamma_{n,m}} \cdot \boldsymbol{\Omega}_{q,n,m}^T \cdot e^{j2\pi f_c \tau_{qp,n,m}(t)} \cdot \delta(\tau - \tau_{qp,n,m}(t)) \cdot \boldsymbol{\Omega}_{p,n,m} \end{aligned} \quad (9)$$

where $\Phi_{n,m}^{\theta\theta}$, $\Phi_{n,m}^{\theta\phi}$, $\Phi_{n,m}^{\phi\theta}$, $\Phi_{n,m}^{\phi\phi}$ are random initial phases with four different combinations of polarization, which are uniform distributions within $[-\pi, \pi]$. Steering vectors of the p th Tx and q th Rx antenna element via the m th ray in the n th cluster are $\boldsymbol{\Omega}_{p,n,m}$ and $\boldsymbol{\Omega}_{q,n,m}$, respectively. The scenario-dependent variable for the m th ray in the n th cluster is denoted as $\gamma_{n,m}$.

In (3) and (9), the CIRs of LoS and NLoS components are dependent on time, space, and frequency. The power of the m th ray from the p th Tx antenna and q th Rx antenna at time t is determined by [17]

$$P'_{qp,n,m}(t) = \exp(-\tau_{qp,n,m}(t) \frac{r_\tau - 1}{r_\tau \cdot DS}) \cdot 10^{\frac{-Z_n}{10}} \cdot \xi_{qp} \quad (10)$$

where r_τ is the delay factor and DS is the root mean square (RMS) delay spread (DS). The cluster shadowing is denoted as a Gaussian distribution Z_n and ξ_{qp} is a lognormal process, which describes the smooth power transition along Tx and Rx antenna arrays. The delay for the m th ray in the n th cluster at time t is

$$\tau_{qp,n,m}(t) = \|\mathbf{d}_{qp,n,m}(t)\|/c + \tilde{\tau}_{n,m} \quad (11)$$

By calculating (13), the distance can be obtained by using second-order approximation $\sqrt{1+x} \approx 1 + x/2$, which is derived as

$$d_{p,n,m}^T(t) \approx \underbrace{d_{n,m}^T - \cos(\omega_p^T) v^T t - \cos(\vartheta^T) \delta_p}_{\text{WSS PWF}} + \underbrace{\frac{\sin^2(\vartheta^T) \delta_p^2}{2d_{n,m}^T} + \frac{\sin^2(\omega_p^T) (v^T t)^2}{2[d_{n,m}^T - \cos(\vartheta^T) \delta_p]}}_{\text{non-stationary SWF}}. \quad (16)$$

The distance contains WSS PWF and non-stationary SWF terms. In this formula, ϑ^T is the angle between Tx antenna array and C_n^T , which can be calculated as

$$\cos(\vartheta^T) = \cos(\theta_{n,m}^T) \cos(\beta_E^T) \cos(\beta_A^T - \phi_{n,m}^T) + \sin(\theta_{n,m}^T) \sin(\beta_E^T). \quad (17)$$

The angle ω_p^T in (16) is the moving direction of the p th Tx antenna to cluster C_n^T , and it can be calculated as [17]

$$\cos(\omega_p^T) = \frac{d_{n,m}^T \cos(\alpha^T - \phi_{n,m}^T) \cos(\theta_{n,m}^T) - \delta_p \cos(\alpha^T - \beta_A^T) \cos(\beta_E^T)}{\left[(d_{n,m}^T)^2 - 2d_{n,m}^T \delta_p \cos(\vartheta^T) + \delta_p^2 \right]^{1/2}}. \quad (18)$$

If the channel has WSS and PWF assumptions, i.e., $v^T t \ll d_{n,m}^T$, $\delta_p \ll d_{n,m}^T$, the non-stationary SWF term in (16) is approximated to zero, and the distance $d_{p,n,m}^T(t)$ can be simplified as

$$d_{p,n,m}^T(t) \approx d_{n,m}^T - \cos(\omega_p^T) v^T t - \cos(\vartheta^T) \delta_p. \quad (19)$$

In this case, the angle in (18) is uncorrelated to the Tx antenna, so it can be written as

$$\cos(\omega_p^T) = \cos(\alpha^T - \phi_{n,m}^T) \cos(\theta_{n,m}^T). \quad (20)$$

For the Rx side, the corresponding formulas can be obtained by replacing superscript T and subscript p with superscript R and subscript q .

The cross-polarization power ratio (XPR) for the m th ray in n th cluster can be calculated as

$$\kappa_{n,m} = 10^{X_{n,m}/10} \quad (21)$$

where $X_{n,m}$ follows Gaussian distribution with mean value μ_{XPR} and standard variance σ_{XPR} .

B. Cluster Evolution

To model non-stationarities in the time and space domains, the cluster birth and death process is proposed in this channel model. Previous work modeled the time and space non-stationarities separately. However, the appearance and disappearance of clusters on the time axis and array axis both obey Poisson distributions, so the birth and death process can be jointly modeled in the

time and space domains [10]. According to the cosine theorem, the cluster survival probability during Δt with antenna distance Δr^T at Tx can be computed as

$$P_{\text{sur}}^T(\Delta t, \Delta r^T) = e^{-\lambda_D [(\epsilon_1^T)^2 + (\epsilon_2^T)^2 - 2\epsilon_1^T \epsilon_2^T \cos(\phi^T - \beta_A^T)]^{\frac{1}{2}}} \quad (22)$$

where λ_D is the death rate of clusters, ϵ_1^T and ϵ_2^T are position differences on the time axis and array axis at the Tx side, respectively. The position difference on the time axis is computed as

$$\epsilon_1^T = \frac{\Delta t}{D_s/v^T} = \frac{v^T \Delta t}{D_s} \quad (23)$$

where D_s is environment-dependent correlation distance on the time axis. The position difference on the array axis is written as

$$\epsilon_2^T = \frac{\Delta r^T \cos(\beta_E^T)}{D_a} \quad (24)$$

where D_a is the correlation distance on the array axis. The values of correlation distances can be determined according to [39].

To model the non-stationarity in the frequency domain, we can generate correlated clusters with different delays [42]. The channel correlation parameter of the m_i th and m_j th clusters at frequency f can be expressed as

$$\rho_{m_i, m_j}(t, f) = \frac{1}{\tau_{m_i}(t) - \tau_{m_j}(t)} \left(\frac{f}{f_c} \right)^\gamma \quad (25)$$

where $\tau_{m_i}(t)$ and $\tau_{m_j}(t)$ are the delays of the m_i th and m_j th clusters, respectively. Then, the cluster survival probability at the Tx side in STF domains is

$$P_{\text{sur}}^T(\Delta t, \Delta r^T, f) = \rho_{m_i, m_j}(t, f) \cdot e^{-\lambda_D [(\epsilon_1^T)^2 + (\epsilon_2^T)^2 - 2\epsilon_1^T \epsilon_2^T \cos(\phi^T - \beta_A^T)]^{\frac{1}{2}}}. \quad (26)$$

The joint survival probability is calculated as

$$P_{\text{sur}}(\Delta t, \Delta r^T, \Delta r^R, f) = P_{\text{sur}}^T(\Delta t, \Delta r^T, f) \cdot P_{\text{sur}}^R(\Delta t, \Delta r^R, f). \quad (27)$$

The mean value of the newly generated cluster number is computed as

$$\mathbb{E}(N_{\text{new}}) = \frac{\lambda_B}{\lambda_D} [1 - P_{\text{sur}}(\Delta t, \Delta r^T, \Delta r^R, f)] \quad (28)$$

where λ_B is the birth rate of clusters.

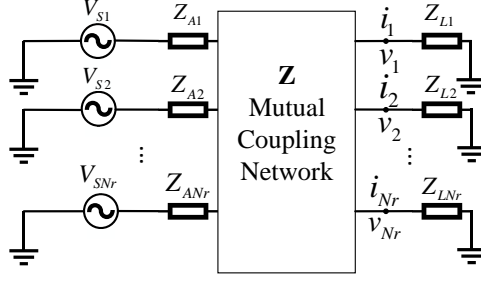


Fig. 3. A multi-port communication model for the mutual coupling network at the Rx side.

C. Mutual Coupling

As antenna elements are located close to each other, there is a portion of energy coupled with adjacent antenna elements, and the MC effect needs to be modeled in the channels, especially in ultra-massive MIMO channels [20]. MC is a physical phenomenon in compact antenna arrays [21]. It is modeled by the electromagnetic theory and circuit theory and is illustrated in Fig. 3. The radiation of the coming wave to the Rx antenna array is equivalent to the effect of an external signal source $V_{S1}, V_{S2}, \dots, V_{SNr}$ on each array antenna element. Here, we use an impedance parameter matrix to represent MC at the Rx side. The signal voltage at the feed point can be expressed as [43]

$$\sum_{j=1}^{N_r} v_j = - \sum_{j=1}^{N_r} (i_j Z_{jj} - v_j^o) \quad (29)$$

where v_j^o is the open circuit voltage of feed point and Z_{jj} is the mutual impedance between two antenna elements. From circuit theory, the voltage is written as $v_j = i_j Z_{Lj}, j = 1, \dots, N_r$. The open circuit voltage vector is expressed as [43]

$$\mathbf{v}^o = (\mathbf{I}_{N_r} + \mathbf{Z}_L^{-1} \mathbf{Z}) \mathbf{v} \quad (30)$$

where \mathbf{I}_{N_r} is $N_r \times N_r$ identity matrix and \mathbf{Z} is the mutual impedance matrix. The load impedance matrix \mathbf{Z}_L is a diagonal matrix with elements of $Z_{L1}, Z_{L2}, \dots, Z_{LN_r}$. The voltage vector of the received signal can be computed as

$$\mathbf{v}_r = (\mathbf{I}_{N_r} + \mathbf{Z}_L^{-1} \mathbf{Z})^{-1} \mathbf{v}^o. \quad (31)$$

The voltage vector of the received signal with MC is $\mathbf{v}_r^c = \mathbf{C}_r \cdot \mathbf{v}_r^{nc}$, and the voltage vector of the received signal without MC is calculated as

$$\mathbf{v}_r^{nc} = (\mathbf{I}_{N_r} + \mathbf{Z}_L^{-1} \mathbf{Z}_A)^{-1} \mathbf{v}^o \quad (32)$$

where the antenna impedance \mathbf{Z}_A is a diagonal matrix with elements of $Z_{A1}, Z_{A2}, \dots, Z_{AN_r}$. Then we can obtain

$$[\mathbf{C}_r - (\mathbf{I}_{N_r} + \mathbf{Z}_L^{-1}\mathbf{Z})^{-1}(\mathbf{I}_{N_r} + \mathbf{Z}_L^{-1}\mathbf{Z}_A)]\mathbf{v}^o = 0. \quad (33)$$

Assume that there are two antennas and the lengths of the first antenna and second antenna are l_1 and l_2 , respectively. The vertical and horizontal distances between the two antennas are h and d , respectively. The open circuit voltage v_2^o of the second antenna can be calculated as [22]

$$v_2^o = \frac{1}{i_2} \left(\int_h^{l_2+h} E_{z1} i_2(z) dz + \int_{l_2+h}^{2l_2+h} E_{z1} i_2(z) dz \right) \quad (34)$$

where i_2 is the base current on antenna 2, and its distribution on the z axis is sinusoidal and can be written as

$$\begin{aligned} i_2(z) &= i_{2m} \sin \beta(z - h) & h < z < l_2 + h \\ i_2(z) &= i_{2m} \sin \beta(2l_2 + h - z) & l_2 + h < z < 2l_2 + h \end{aligned} \quad (35)$$

where i_{2m} is the maximum current of $i_2(z)$ and $\beta = 2\pi/\lambda$ is the phase constant. The parallel electric intensity component E_{z1} at point z on the second antenna is induced by the first antenna, which is calculated as [44]

$$E_{z1} = 30i_{1m} \left[\frac{-je^{-j\beta r_1}}{r_1} + \frac{-je^{-j\beta r_2}}{r_2} + \frac{2j \cos \beta l_1 e^{-j\beta r_0}}{r_0} \right] \quad (36)$$

where r_1 , r_2 , and r_0 are the distances between the point z on the second antenna and the top, bottom, and middle of the first antenna.

In (30), the mutual impedance matrix \mathbf{Z} is defined in [22] with different antenna topologies. The self-impedance is the diagonal element of \mathbf{Z} , while the non-diagonal element is the mutual impedance between different antenna elements. According to the reciprocity theorem, the mutual impedance between two antennas can be computed as

$$\begin{aligned} Z_{12} = Z_{21} &= -\frac{i_1 i_2}{i_{1m} i_{2m}} \cdot \frac{v_2^o}{i_1} = -30 \left[\left(\int_h^{l_2+h} \sin \beta(z - h) + \int_{l_2+h}^{2l_2+h} \sin \beta(2l_2 + h - z) \right) \right. \\ &\quad \left. \left(\frac{-je^{-j\beta r_1}}{r_1} + \frac{-je^{-j\beta r_2}}{r_2} + \frac{2j \cos \beta l_1 e^{-j\beta r_0}}{r_0} \right) dz \right]. \end{aligned} \quad (37)$$

When two antennas are in a non-staggered or colinear arrangement with the same length, the mutual resistance R_{12} and reactance X_{12} can be calculated using closed-form expressions [22]. Therefore, the mutual impedance is written as

$$Z_{12} = R_{12} + jX_{12}. \quad (38)$$

The self-impedance is defined as

$$Z_{11} = \frac{V_1}{I_1} \Big|_{I_2=0}, \quad Z_{22} = \frac{V_2}{I_2} \Big|_{I_1=0} \quad (39)$$

where V_1 and V_2 are induced voltages generated by the currents I_1 and I_2 on antennas 1 and 2, respectively. Under this condition, Z_{11} and Z_{22} are the exact meanings of antenna input impedance. For the load impedance \mathbf{Z}_L , it is optimized for capacity maximization using the single-port matching method [46]. For other antenna arrangements, the impedance matrix can be obtained by utilizing electromagnetic calculation methods.

D. Antenna Efficiency

MC has a relationship with antenna efficiency, which is related to antenna spacing. When the element spacing is less than half-wavelength, the antenna efficiency of each element at the Rx can be calculated as [45]

$$\eta_q(\delta_q) = \frac{\pi L_{r,x} L_{r,y}}{N_r \lambda^2} = \frac{\pi \delta_q^2}{\lambda^2} \quad (40)$$

where $L_{r,x}$ and $L_{r,y}$ are the length and width of antenna array at the Rx side, respectively. In addition, the antenna efficiency for more complicated antenna arrays may need to use the full-wave simulation to obtain, which is given as

$$\eta_q = \frac{P_T - P_{q,loss}}{P_T} \quad (41)$$

where P_T is transmit power and $P_{q,loss}$ is return loss power of the q th port, which can be obtained in the full-wave simulation software. By calculating (33), the MC matrix considering antenna efficiency at the Rx side is

$$\mathbf{C}_r = \text{diag}(\mathbf{\Gamma}_r) (\mathbf{I}_{N_r} + \mathbf{Z}_L^{-1} \mathbf{Z})^{-1} (\mathbf{I}_{N_r} + \mathbf{Z}_L^{-1} \mathbf{Z}_A) \quad (42)$$

where $\text{diag}(\mathbf{\Gamma}_r)$ is the diagonal matrix of antenna efficiency, i.e., $[\mathbf{\Gamma}_r]_{q,q} = \eta_q$. The MC matrix \mathbf{C}_t at Tx can be obtained similarly.

E. Antenna Steering Vectors

The typical antenna array topologies include ULA, UPA, and UCA. Steering vectors are used to estimate the direction of angle and are usually applied to positioning and beamforming [30]. Under different antenna topologies, steering vectors have different forms. The illustrations of

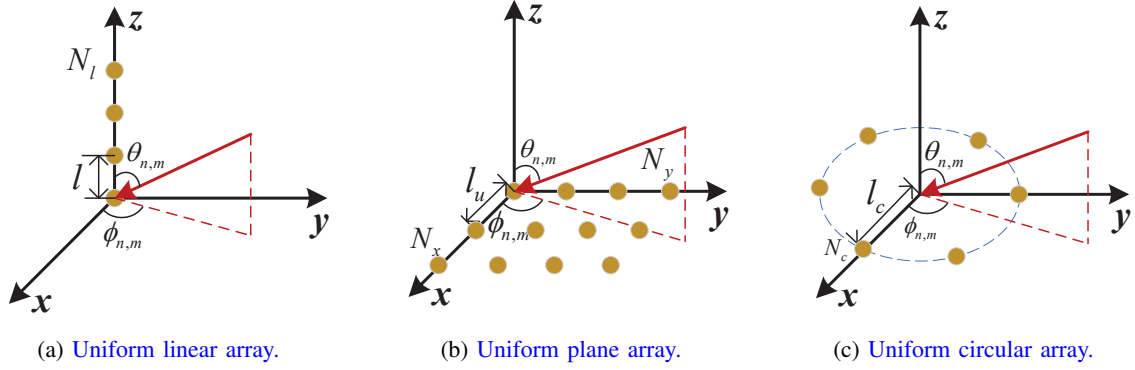


Fig. 4. The illustrations of steering vectors for (a) uniform linear array, (b) uniform plane array, and (c) uniform circular array.

ULA, UPA, and UCA steering vectors are shown in Fig. 4. The steering vectors at the Rx side in the far field can be obtained as follows.

1) ULA

The distance between two adjacent antenna elements is l , and the number of antenna elements is N_l . The steering vector of ULA via the m th ray in the n th cluster is calculated as

$$\mathbf{\Omega}_{q,n,m} = \frac{1}{\sqrt{N_l}} [1, e^{-j\frac{2\pi}{\lambda} l \cos \theta_{n,m}^R}, \dots, e^{-j\frac{2\pi}{\lambda} (N_l-1) l \cos \theta_{n,m}^R}]^T. \quad (43)$$

2) UPA

The number of antenna elements in UPA is $N_x \times N_y$ and the distance between two adjacent elements is l_u . The steering vector of UPA via the m th ray in the n th cluster is calculated as

$$\mathbf{\Omega}_{n,m} = \frac{1}{\sqrt{N_x N_y}} [1, e^{-j\frac{2\pi}{\lambda} l_u \sin \theta_{n,m}^R (\cos \phi_{n,m}^R + \sin \phi_{n,m}^R)}, \dots, e^{-j\frac{2\pi}{\lambda} l_u \sin \theta_{n,m}^R ((N_x-1) \cos \phi_{n,m}^R + (N_y-1) \sin \phi_{n,m}^R)}]^T. \quad (44)$$

3) UCA

The number of antenna elements in UCA is N_c and the distance between antenna elements and the origin is l_c . The steering vector of UCA via the m th ray in the n th cluster is written as

$$\mathbf{\Omega}_{n,m} = \frac{1}{\sqrt{N_c}} [1, e^{-j\frac{2\pi}{\lambda} l_c \sin \theta_{n,m}^R \cos(\phi_{n,m}^R - \frac{2\pi}{N_c})}, \dots, e^{-j\frac{2\pi}{\lambda} l_c \sin \theta_{n,m}^R \cos(\phi_{n,m}^R - \frac{2\pi}{N_c} (N_c-1))}]^T. \quad (45)$$

In the near field, we assume that there are M antenna elements in an array, and the source signal is in the near field of the array. Take the center of the antenna array as the origin of the coordinate system, the distance between the source signal and the origin is r . The schematic diagram of the Rx array element in the near field with arbitrary structure is shown in Fig. 5.

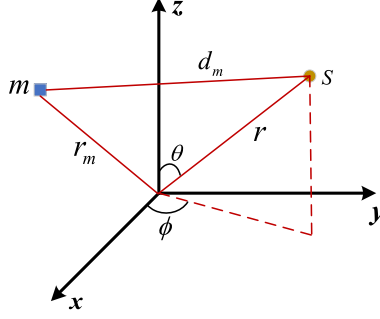


Fig. 5. The schematic diagram of the Rx array element in the near field with arbitrary structures.

Assume that the position of the m th element is (x_m, y_m, z_m) and the distance vector to the origin is \mathbf{r}_m . The distance between the m th element and the k th source is calculated as

$$d_{m,k} = \|\mathbf{r}_k - \mathbf{r}_m\| = [(r_k \sin \theta \sin \phi - x_m)^2 + (r_k \sin \theta \cos \phi - y_m)^2 + (r_k \cos \theta - z_m)^2]^{1/2}. \quad (46)$$

The receiving signals at the origin are set as the reference signals. The steering vector in the near field can be derived as

$$\boldsymbol{\Omega}_{\text{NF}} = \left[1, \frac{r_k}{d_{1,k}} e^{-jk(d_{1,k}-r_k)}, \dots, \frac{r_k}{d_{M-1,k}} e^{-jk(d_{M-1,k}-r_k)} \right]^T. \quad (47)$$

If the signal is wideband, the receiving array signals are wideband signals containing multi-frequency components. Therefore, the steering vector is a function of frequency f , which is written as

$$\boldsymbol{\Omega}_{\text{NF}}(f) = \left[1, \frac{r_k}{d_{1,k}} e^{-j\frac{2\pi f}{c}(d_{1,k}-r_k)}, \dots, \frac{r_k}{d_{M-1,k}} e^{-j\frac{2\pi f}{c}(d_{M-1,k}-r_k)} \right]^T \quad (48)$$

which can be used in the near-field region with arbitrary antenna topologies in wideband communication systems.

III. STATISTICAL PROPERTIES AND CHANNEL CAPACITIES

A. STF Correlation Functions

Statistical properties are calculated by the channel transfer function (CTF), which is the Fourier transform of CIR w.r.t. delay τ . The CTF of the proposed channel model can be written as

$$H_{qp}(t, f) = \int_{-\infty}^{\infty} h_{qp,fc}(t, \tau) e^{-j2\pi f\tau} d\tau = \sqrt{\frac{K_R(t)}{K_R(t) + 1}} H_{qp}^{\text{LoS}}(t, f) + \sqrt{\frac{1}{K_R(t) + 1}} H_{qp}^{\text{NLoS}}(t, f). \quad (49)$$

The LoS component of the CTF can be calculated as

$$H_{qp}^{\text{LoS}}(t, f) = h_{qp, f_c}^{\text{LoS}}(t, \tau) \cdot e^{-j2\pi f \tau_{qp}^L(t)} \quad (50)$$

and the NLoS component can be written as

$$H_{qp}^{\text{NLoS}}(t, f) = h_{qp, f_c}^{\text{NLoS}}(t, \tau) \cdot e^{-j2\pi f \tau_{qp, n, m}(t)}. \quad (51)$$

From (49), the STF correlation function can be computed as

$$R_{qp, \tilde{q}\tilde{p}}(t, f; \Delta t, \Delta f, \Delta \mathbf{r}) = \mathbb{E}\{H_{qp}(t, f)H_{\tilde{q}\tilde{p}}^*(t + \Delta t, f + \Delta f)\} \quad (52)$$

where $\mathbb{E}\{\cdot\}$ is the expectation operator and $\{\cdot\}^*$ is the complex conjugate operator. The subscript $\tilde{q}\tilde{p}$ is the antenna pair between the \tilde{p} th Tx and \tilde{q} th Rx. In addition, $\Delta \mathbf{r}$ includes Δr^T and Δr^R , which are distance between p th and \tilde{p} th antenna and distance between q th and \tilde{q} th antenna, respectively. By substituting (49) into (52), the STF correlation functions is obtained as

$$\begin{aligned} R_{qp, \tilde{q}\tilde{p}}(t, f; \Delta t, \Delta f, \Delta \mathbf{r}) &= \sqrt{\frac{K_R(t)}{K_R(t) + 1}} \cdot \sqrt{\frac{K_R(t + \Delta t)}{K_R(t + \Delta t) + 1}} R_{qp, \tilde{q}\tilde{p}}^{\text{LoS}}(t, f; \Delta t, \Delta f, \Delta \mathbf{r}) \\ &+ \sqrt{\frac{1}{K_R(t) + 1}} \cdot \sqrt{\frac{1}{K_R(t + \Delta t) + 1}} R_{qp, \tilde{q}\tilde{p}}^{\text{NLoS}}(t, f; \Delta t, \Delta f, \Delta \mathbf{r}). \end{aligned} \quad (53)$$

Here, the correlation function of LoS component is

$$R_{qp, \tilde{q}\tilde{p}}^{\text{LoS}}(t, f; \Delta t, \Delta f, \Delta \mathbf{r}) = h_{qp, f_c}^{\text{LoS}}(t, \tau) h_{\tilde{q}\tilde{p}, f_c + \Delta f}^{\text{LoS}*}(t + \Delta t, \tau) \cdot e^{j2\pi[(f + \Delta f)\tau_{\tilde{q}\tilde{p}}^L(t + \Delta t) - f\tau_{qp}^L(t)]} \quad (54)$$

and the correlation function of NLoS component is written as

$$R_{qp, \tilde{q}\tilde{p}}^{\text{NLoS}}(t, f; \Delta t, \Delta f, \Delta \mathbf{r}) = h_{qp, f_c}^{\text{NLoS}}(t, \tau) h_{\tilde{q}\tilde{p}, f_c + \Delta f}^{\text{NLoS}*}(t + \Delta t, \tau) \cdot e^{j2\pi[(f + \Delta f)\tau_{\tilde{q}\tilde{p}, n, m}(t + \Delta t) - f\tau_{qp, n, m}(t)]}. \quad (55)$$

Clusters experience birth and death processes due to STF non-stationarities, so the correlation of NLoS component needs to be further expanded as

$$\begin{aligned} R_{qp, \tilde{q}\tilde{p}}^{\text{NLoS}}(t, f; \Delta t, \Delta f, \Delta \mathbf{r}) &= P_{\text{sur}}(\Delta t, \Delta r^T, \Delta r^R, f) \cdot h_{qp, f_c}^{\text{NLoS}}(t, \tau) h_{\tilde{q}\tilde{p}, f_c + \Delta f}^{\text{NLoS}*}(t + \Delta t, \tau) \\ &\cdot e^{j2\pi[(f + \Delta f)\tau_{\tilde{q}\tilde{p}, n, m}(t + \Delta t) - f\tau_{qp, n, m}(t)]} \end{aligned} \quad (56)$$

where $P_{\text{sur}}(\Delta t, \Delta r^T, \Delta r^R, f)$ represents the joint survival probability in STF domains. From the STF correlation function, the temporal autocorrelation function (ACF) can be obtained by imposing $\Delta f = 0, \Delta r^T = 0, \Delta r^R = 0, \tilde{p} = p, \tilde{q} = q$, which is expressed as

$$R_{qp}(t, f; \Delta t) = \mathbb{E}\{H_{qp}(t, f)H_{qp}^*(t + \Delta t, f)\} = \sqrt{\frac{K_R(t)}{K_R(t) + 1}} \cdot \sqrt{\frac{K_R(t + \Delta t)}{K_R(t + \Delta t) + 1}} R_{qp}^{\text{LoS}}(t, f; \Delta t) + \sqrt{\frac{1}{K_R(t) + 1}} \cdot \sqrt{\frac{1}{K_R(t + \Delta t) + 1}} R_{qp}^{\text{NLoS}}(t, f; \Delta t). \quad (57)$$

The temporal ACF of the LoS component is computed as

$$R_{qp}^{\text{LoS}}(t, f; \Delta t) = h_{qp,fc}^{\text{LoS}}(t, \tau)h_{qp,fc}^{\text{LoS}*}(t + \Delta t, \tau) \cdot e^{j2\pi f[\tau_{qp}^L(t+\Delta t) - \tau_{qp}^L(t)]} \quad (58)$$

and the temporal ACF of the NLoS component is written as

$$R_{qp}^{\text{NLoS}}(t, f; \Delta t) = P_{\text{sur}}(\Delta t) \cdot h_{qp,fc}^{\text{NLoS}}(t, \tau)h_{qp,fc}^{\text{NLoS}*}(t + \Delta t, \tau) \cdot e^{j2\pi f[\tau_{qp,n,m}(t+\Delta t) - \tau_{qp,n,m}(t)]} \quad (59)$$

where $P_{\text{sur}}(\Delta t)$ is separately modeled as a birth and death process and can be calculated as

$$P_{\text{sur}}(\Delta t) = e^{-\lambda_D \frac{P_F(\Delta v^R + \Delta v^T)\Delta t}{D_s}} \quad (60)$$

where P_F is the probability of the moving cluster. The spatial CCF is obtained by setting $\Delta t = 0, \Delta f = 0$. Similarly, the frequency correlation function (FCF) is computed by imposing $\Delta t = 0, \Delta r^T = 0, \Delta r^R = 0, \tilde{p} = p, \tilde{q} = q$. From the derivation, the correlation functions are not only related to the STF differences, but also depend on STF instances, which demonstrates the STF non-stationary properties of the proposed channel model.

B. Power Spectral Density

The power spectral density (PSD) characterizes the power distribution along the STF domains, which includes angular PSD, Doppler PSD, and delay PSD. The Doppler PSD can be obtained from the Fourier transform of temporal ACF w.r.t. time difference Δt , which is written as

$$S_{qp}(t, f; f_d) = \int_0^\infty R_{qp}(t, f; \Delta t)e^{-j2\pi f_d \Delta t} d\Delta t \quad (61)$$

where f_d is the Doppler frequency. The delay PSD is the inverse Fourier transform of the FCF w.r.t. frequency difference Δf , which can be computed as

$$S_{qp}(t, f; \tau) = \int_0^\infty R_{qp}(t, f; \Delta f)e^{j2\pi \Delta f \tau} d\Delta f. \quad (62)$$

The angular PSD at the Rx side is the Fourier transform of spatial CCF w.r.t. space difference Δr^R , which is calculated as

$$S_{qp}(t, f; \Omega^R) = \int_0^\infty R_{qp, \tilde{qp}}(t, f; \Delta r^R) e^{-j2\pi \Delta r^R \Omega^R} d\Delta r^R \quad (63)$$

where Ω^R denotes the angle at the Rx side. In short, the PSDs in STF domains can be obtained by the Fourier transform or inverse Fourier transform of correlation functions.

C. More Statistical Properties

From the temporal ACF, the spatial CCF, and the FCF, the coherence time, coherence distance, and coherence bandwidth can be obtained. For example, the coherence time is the smallest positive value of time difference Δt that satisfy the condition $|R_{qp}(t, f; \Delta t)| = \frac{1}{2}|R_{qp}(t, f; 0)|$. The coherence time is denoted as $T_c = \Delta t$. The coherence distance D_c and coherence bandwidth B_c are obtained similarly from the STF correlation functions.

From the Doppler PSD in (61), the average Doppler shift μ_{f_d} and RMS Doppler spread σ_{f_d} can be obtained. From the delay PSD in (62), the average delay μ_τ and RMS DS σ_τ can be calculated. Similarly, from angular PSD in (63), the average angle μ_Ω and RMS angular spread σ_Ω are obtained. For instance, the average delay can be computed as

$$\mu_\tau = \frac{\int_0^\infty \tau S_{qp}(t, f; \tau) d\tau}{\int_0^\infty S_{qp}(t, f; \tau) d\tau}. \quad (64)$$

The RMS DS can be calculated as

$$\sigma_\tau = \sqrt{\frac{\int_0^\infty (\tau - \mu_\tau)^2 S_{qp}(t, f; \tau) d\tau}{\int_0^\infty S_{qp}(t, f; \tau) d\tau}}. \quad (65)$$

The average delay and RMS DS are the first moment and second central moment of the delay PSD, respectively.

D. Non-Stationary Channel Capacity Calculation Method

Channel capacities of massive MIMO channel models depend on the knowledge of CSI at the Tx and Rx. When the CSI is known to the Rx and unknown to the Tx, the conventional ergodic channel capacity can be calculated as

$$C = \mathbb{E} \left\{ \log_2 \det \left(\mathbf{I} + \frac{\rho}{N_t} \mathbf{H} \mathbf{H}^H \right) \right\} \quad (66)$$

where $\det\{\cdot\}$ is the determinant operator and ρ is the signal-to-noise ratio (SNR). However, this formula ignores STF non-stationarities of channel models, which cannot apply to non-stationary

channel models. Here, we use the definition of SI to divide the non-stationary channel into WSS sub-channels. In each SI, the channel can be considered as WSS. The normalized ACF of delay PSD is calculated as [10]

$$R_{\Lambda}(t, f; \Delta t, \Delta f, \Delta \mathbf{r}) = \frac{\int S_{qp}(t, f; \tau) S_{qp}(t + \Delta t, f + \Delta f; \tau) d\tau}{\max\{\int S_{qp}(t, f; \tau)^2 d\tau, \int S_{qp}(t + \Delta t, f + \Delta f; \tau)^2 d\tau\}}. \quad (67)$$

The SI in the time domain is the maximum time that the ACF of delay PSD is higher than a threshold c_{th} , which is written as

$$I(t) = \inf \{ \Delta t \mid R_{\Lambda}(t, f; \Delta t, \Delta f = 0, \Delta \mathbf{r} = 0) \leq c_{th} \} \quad (68)$$

where $\inf\{\cdot\}$ is the infimum function. Similarly, the SI in the space domain can be obtained as

$$D(r) = \inf \{ \Delta r \mid R_{\Lambda}(t, f; \Delta t = 0, \Delta f = 0, \Delta \mathbf{r}) \leq c_{th} \} \quad (69)$$

and SI in the frequency domain is expressed as

$$B(f) = \inf \{ \Delta t \mid R_{\Lambda}(t, f; \Delta t = 0, \Delta f, \Delta \mathbf{r} = 0) \leq c_{th} \}. \quad (70)$$

From the SI, the non-stationary channel can be divided into S WSS sub-channels [47]. The non-stationary channel capacities are the summation of the S WSS sub-channel capacities. Therefore, the non-stationary channel capacity can be calculated as

$$C = \mathbb{E} \left\{ \frac{1}{S} \sum_{i,j=1}^S \log_2 \det \left(\mathbf{I} + \frac{\rho}{N_t} \mathbf{R}_{i,j} \mathbf{H}_i \mathbf{H}_i^H \right) \right\} \quad (71)$$

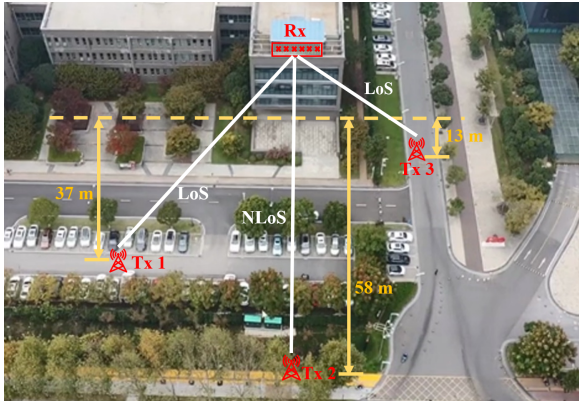
where \mathbf{H}_i is the i th WSS sub-channel with MC and $\mathbf{R}_{i,j} = \mathbb{E}[\mathbf{H}_i \mathbf{H}_j^H]$ is the channel correlation matrix between the i th and j th WSS sub-channel. From the channel measurements, the CSI can be obtained by space-alternating generalized expectation-maximization (SAGE) algorithm [48], so the CSI is known to the Tx and Rx. Then, the spatio-temporal water-filling (WF) algorithm is used to calculate the channel capacity, which is [38]

$$C = \sum_{n=1}^K \log_2 \left(1 + \frac{\lambda_{Z,n} |\lambda_{H,n}|^2}{\sigma^2} \right) \quad (72)$$

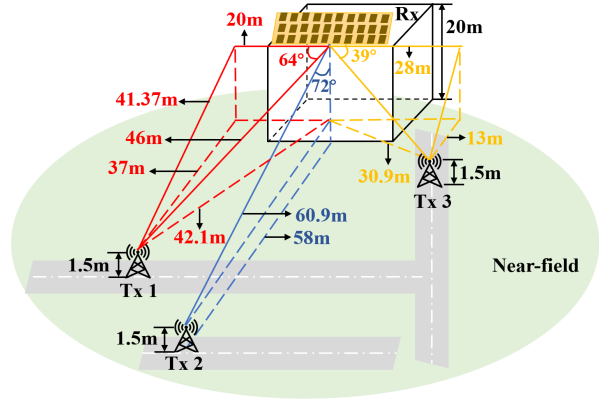
where K and $\lambda_{H,n}$ are the rank and the n th singular value of channel matrix, respectively. The variance of signal noise is σ^2 and the eigenvalue of input signal $Z(t)$ is $\lambda_{Z,n}$, which is the solution of spatio-temporal WF algorithm [38]

$$\lambda_{Z,n} = \left(\xi - \frac{\sigma^2}{|\lambda_{H,n}|^2} \right)^+ \quad (73)$$

where $(\cdot)^+$ equals to zero if the argument is negative and equals to the argument if the argument is positive and ξ denotes the Lagrange multiplier.



(a) Real measurement environment.



(b) Sketch map of channel measurements.

Fig. 6. (a) Real measurement environment and (b) sketch map of the outdoor ultra-massive MIMO scenario.

IV. RESULTS AND ANALYSIS

The ultra-massive MIMO channel measurement campaigns are carried out in an outdoor urban micro-cell (UMi) scenario. The statistical properties and channel capacities of the proposed channel model and channel measurements are studied in this section.

A. Channel Measurement Campaigns

The channel measurement environments and the sketch map of the ultra-massive MIMO scenario are shown in Fig. 6. This measurement campaign was conducted in the China Network Valley. The channel measurement frequency f_c is set at 5.3 GHz and the bandwidth B is 160 MHz. There are 8 omni-directional antennas with 0.88λ antenna spacing equipped at the Tx side and 128 elements in ULA with 0.6λ antenna spacing are placed at the Rx side. There are 4 switch boxes at the Rx and they can receive 4 parallel signals. Each switch box is capable of receiving 32 serial signals, thus a total of 128 channels can be measured. The antenna on each channel is composed of 8 vertical omni-directional patch antennas, which are used for vertical beamforming. The aperture of the ULA is 4.32 m and the Rayleigh distance is 659 m. There are three Tx locations and one Rx location, where Tx1 and Tx3 are in the LoS conditions and Tx2 is in the NLoS condition. They are all located in the near-field region of Rx antenna arrays. Parameters of channel environments are shown in Fig. 6(b).

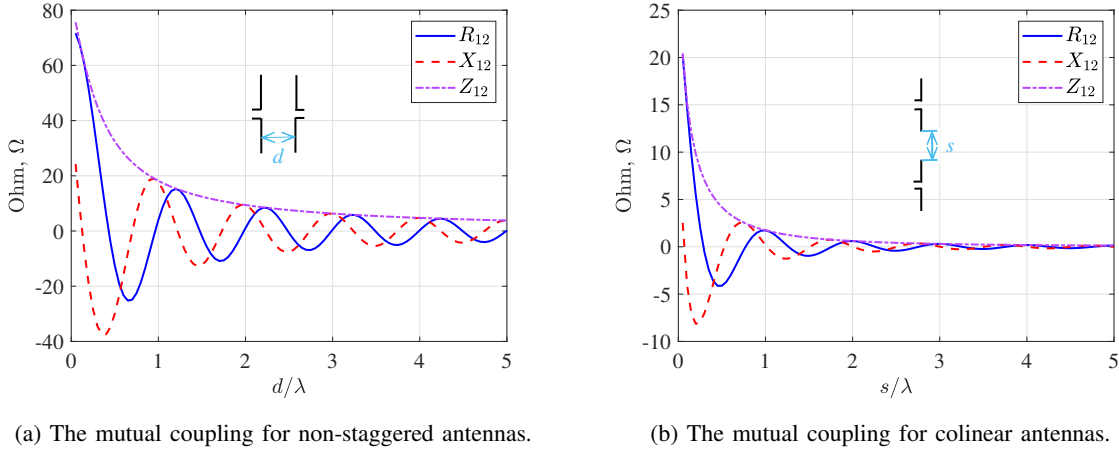
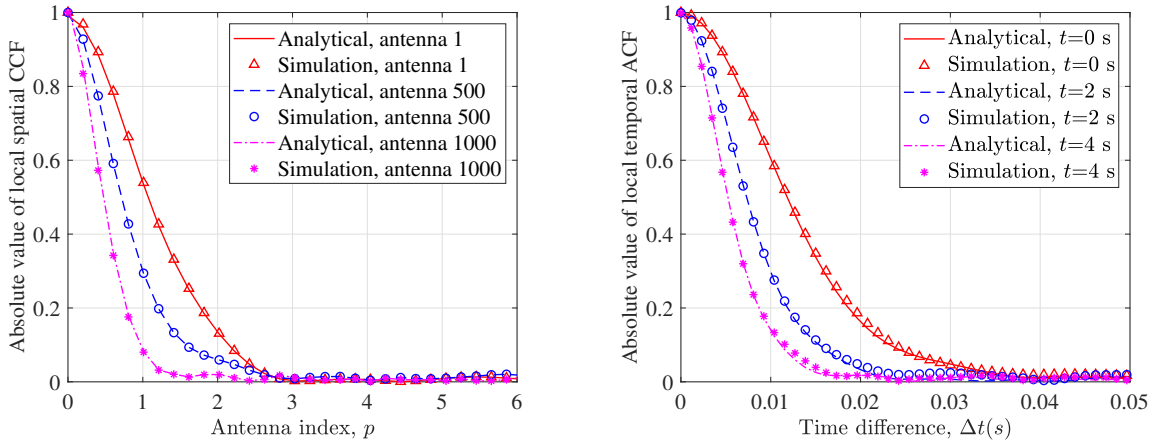


Fig. 7. The resistance, reactance, and mutual impedance of mutual coupling for (a) non-staggered and (b) colinear antenna arrangements ($l_1 = l_2 = \lambda/4$, $f_c = 5.3$ GHz, $c = 3 \times 10^8$ m/s).

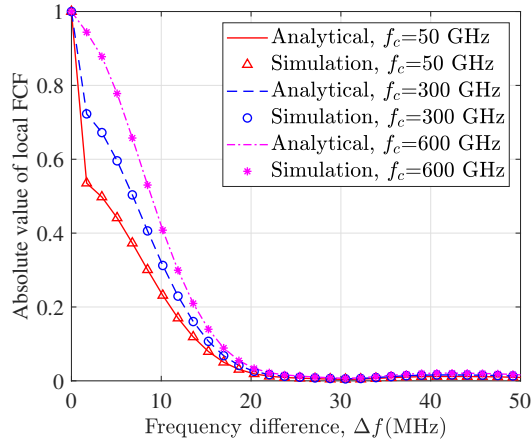
B. Statistical Properties

The simulation parameters are setting as: $N_t = 8$, $N_r = 128$, $\lambda_B = 40/m$, $\lambda_D = 2/m$, $v^{T(R)} = 10$ m/s, $D_s = D_a = 10$ m, $D = 200$ m, $\beta_A^T = \pi/6$, $\beta_E^T = 0$, $\beta_A^R = 0$, $\beta_E^R = 7\pi/18$, $\sigma_{fd} = 3$, $\sigma_\tau = 4$, $\sigma_\Omega = 5$, and other parameters are set according to 3GPP TR 38.901 channel model [39]. In Fig. 7, the mutual resistance R_{12} , mutual reactance X_{12} , and mutual impedance Z_{12} of MC for non-staggered and colinear antenna arrangements are shown. The MC is larger when the distances of antenna elements are smaller, especially when the distances are within λ . In this channel measurement campaign, the MC matrix is only considered at the Rx side since it has smaller antenna spacing. The MC matrix at the Tx side is represented as an identity matrix. The STF correlation functions of the proposed channel model are illustrated in Fig. 8. The STF correlation functions are not only dependent on the STF instant values, but also related to STF differences, which shows the channel STF non-stationarities. **The analytical results were obtained through the plot of the theoretical derivation results of the STF correlation functions according to (53), while the simulation results were obtained by simulating the correlation functions of the channel starting from the impulse response.** The analytical results are in accordance with the simulation results, which demonstrates the correctness of derivation and the accuracy of the proposed channel model.

The coherence distance and Doppler PSD are simulated in Figs. 9 and 10 to optimize the parameter β_E^R in the proposed channel model. The results show that when the angle $\beta_E^R = 70.285^\circ$,



(a) Spatial cross-correlation function at different antenna elements. (b) Temporal autocorrelation function at different time instants.



(c) Frequency correlation function at different carrier frequencies.

Fig. 8. (a) Spatial cross-correlation function at different antenna elements, (b) Temporal autocorrelation function at different time instants, and (c) Frequency correlation function at different carrier frequencies of the non-stationary channel model ($N_t = 8$, $N_r = 1024$, $\lambda_B = 40$ /m, $\lambda_D = 2$ /m, $v^{T(R)} = 10$ m/s, and $\gamma = 30$).

the simulation fits the measurement data better. The optimization of other channel parameters can also be determined by minimizing the RMS error between simulations and measurements. In Fig. 11, the analytical, simulated, and measured spatial CCFs of the channel model with MC and without MC are shown. The spatial CCF with MC is higher than that without MC, which illustrates that MC can increase the spatial CCF because adjacent antennas have a portion of energy from each other. The spatial CCF with MC is closest to the measurement, which means

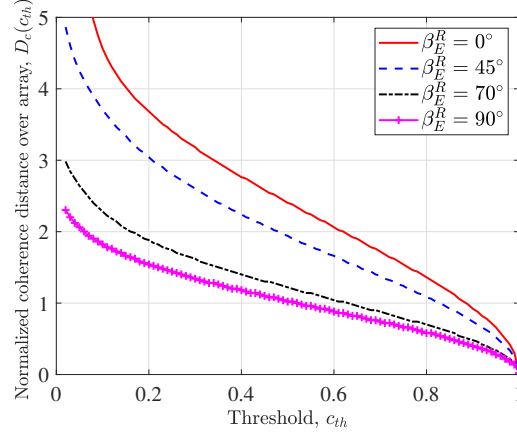


Fig. 9. Normalized coherence distances of the non-stationary channel model with different elevation angles of the Rx array.

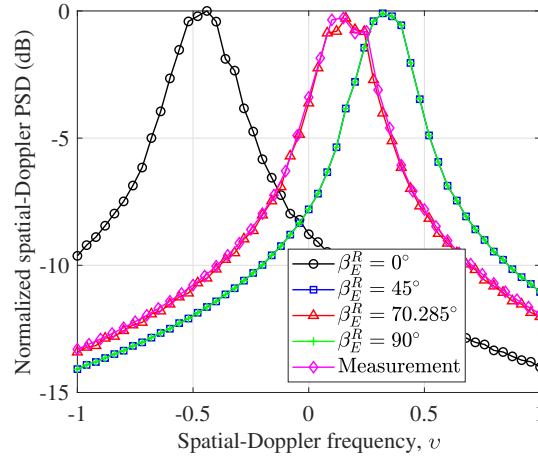


Fig. 10. Simulated and measured Doppler power spectral densities of the non-stationary channel model with different elevation angles of the Rx array.

MC needs to be considered in massive MIMO channel models.

The angular PSDs of Tx1, Tx2, and Tx3 in channel measurements are shown in Fig. 12. Here, the powers of antennas are obtained from channel measurements. The measured angular PSDs can be fitted with the Laplace distribution, which demonstrates the angle of arrival (AoA) distribution is likely to be the Laplace distribution for outdoor propagation in urban areas [13]. The AoAs of Tx1 and Tx3 are about 26° and -40° , respectively. They are almost the same as the channel measurement environments. However, the AoA of Tx2 is different from the environment due to the trees located around Tx2.

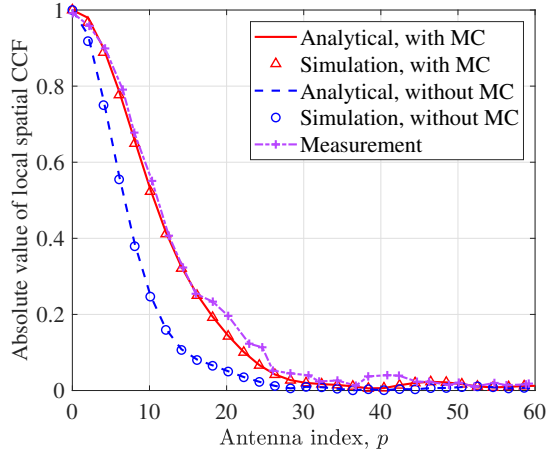
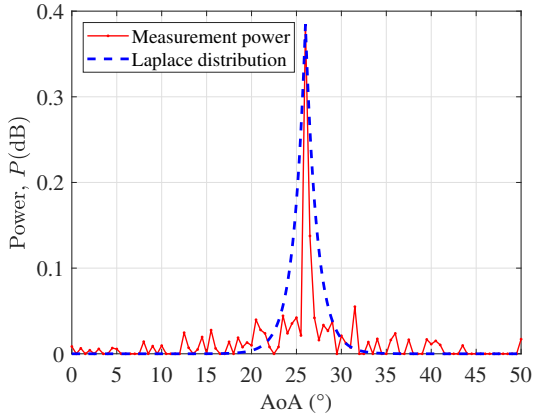


Fig. 11. Analytical, simulated, and measured spatial cross-correlation functions with and without mutual coupling ($f_c = 5.3$ GHz, $B = 160$ MHz, $v^{T(R)} = 0$, $D = 58$ m, $\beta_A^T = 30^\circ$, $\beta_E^T = 0$, $\beta_A^R = 0$, and $\beta_E^R = 70.285^\circ$).

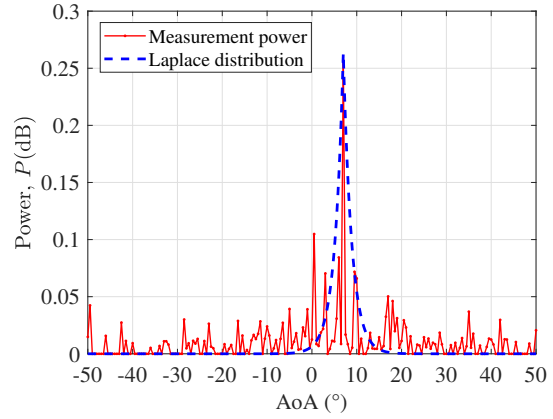
C. Channel Capacities

Channel capacities of different antenna topologies such as ULA, UPA, and UCA are compared in Fig. 13. In the same antenna elements and spacing situation, UCA has the largest channel capacity, which is because UCA has a larger aperture and has more angle information than UPA and ULA. In the same antenna aperture situation, UPA has the largest channel capacity, which illustrates that UPA is the trade-off in terms of physical aperture and channel capacity. The novel non-stationary channel capacity calculation method influenced by the spatial SI is analyzed as follows. The spatial SI can be obtained from Fig. 11, and the value at the Rx is about 8 antennas when the threshold is set to 0.8, so the number of WSS sub-channels can be calculated as 16. Non-stationary channel capacities are calculated by (71). Channel capacities of different numbers of WSS sub-channels are illustrated in Fig. 14. The results show that channel capacities increase with the increasing number of WSS sub-channels, which means the conventional Shannon capacity calculation method underestimates the true channel capacity in non-stationary channels. However, non-stationary channel capacities reach the maximum when the number of sub-channels equals the segments of the spatial SI, which verifies that sub-channels are WSS in each SI. In the time and frequency domains, the temporal and frequency non-stationary channel capacities can be obtained similarly.

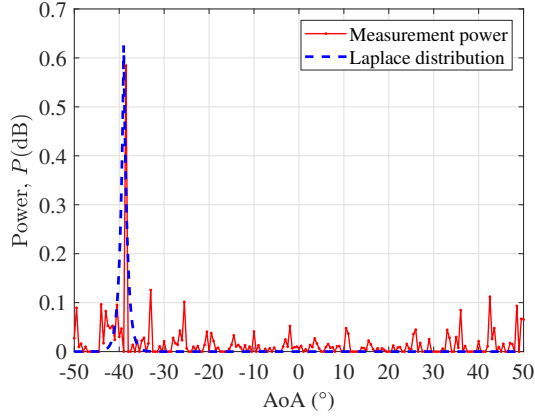
The simulated and measured channel capacities calculated using the novel non-stationary calculation method considering and without considering MC are described in Fig. 15. [Scenario 1](#)



(a) The angular power spectral density of Tx1.



(b) The angular power spectral density of Tx2.

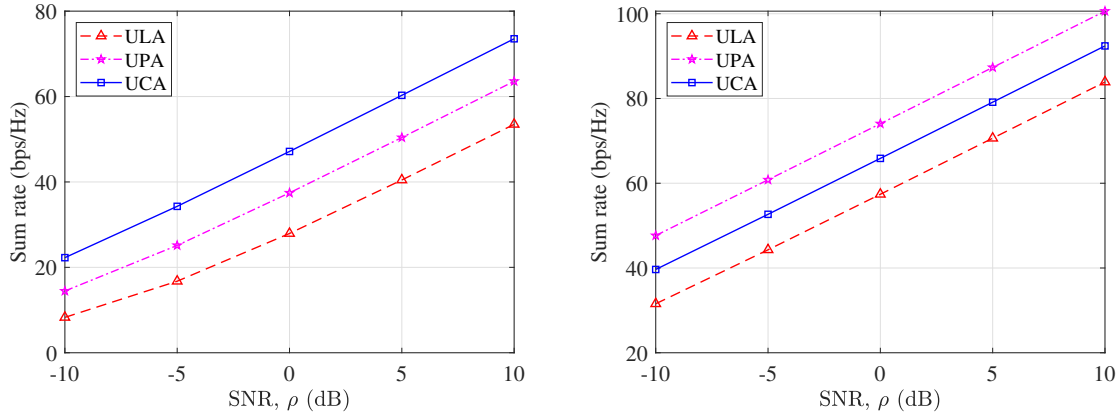


(c) The angular power spectral density of Tx3.

Fig. 12. Measured angular power spectral densities and fitted Laplace distributions of (a) Tx1, (b) Tx2, and (c) Tx3 ($f_c = 5.3$ GHz, $B = 160$ MHz, $v^{T(R)} = 0$, $D = 58$ m, $\beta_A^T = 30^\circ$, $\beta_E^T = 0$, $\beta_A^R = 0$, and $\beta_E^R = 70.285^\circ$).

is the outdoor ultra-massive MIMO with Tx2 and Rx in Fig. 6(a), and scenario 2 is the indoor theater channel measured in [49]. It shows that the simulated capacity considering MC is close to the measured capacity. The simulated capacity without considering MC is higher than that of the measurement and overestimates the channel capacity. This illustrates the correctness of the novel channel capacity calculation method and the necessity of adding the MC effect in non-stationary massive MIMO channel models.

In Fig. 16, simulated and measured channel capacities are calculated by the WF algorithm in (72) and without the WF algorithm. The result shows that when the SNR is large, the channel capacity using the WF algorithm is larger than the channel capacity without using the WF algorithm. The simulated capacity using the WF algorithm is in agreement with the measured



(a) Channel capacities with the same number of antenna elements and spacing. (b) Channel capacities with the same antenna aperture.

Fig. 13. Channel capacities of different antenna topologies with (a) the same number of antenna elements and spacing: $N_l = 8, N_x = 2, N_y = 4, N_c = 8, l = l_u = l_c = \lambda/2$, and (b) the same antenna aperture: $N_c = 64, l_c = 5\lambda$ ($f_c = 5.3$ GHz, $B = 160$ MHz, $\lambda_B = 40/m, \lambda_D = 2/m, v^{T(R)} = 0, \gamma = 0, \beta_A^T = 30^\circ, \beta_A^R = 0, \beta_E^T = 0$, and $\beta_E^R = 70.285^\circ$).

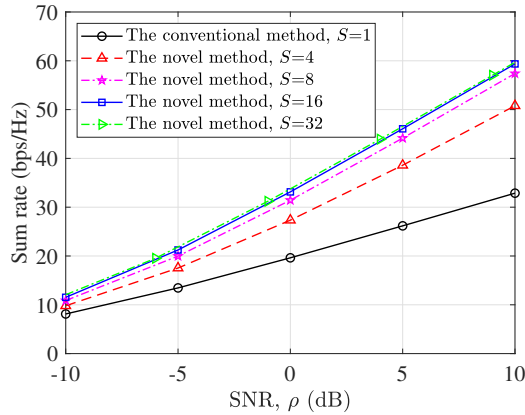


Fig. 14. Channel capacities of the non-stationary channel model with different numbers of wide-sense stationary sub-channels ($N_t = 8, N_r = 128, f_c = 5.3$ GHz, $B = 160$ MHz, $\lambda_B = 40/m, \lambda_D = 2/m, v^{T(R)} = 10$ m/s, $\gamma = 10, \beta_A^T = 30^\circ, \beta_A^R = 0, \beta_E^T = 0$, and $\beta_E^R = 70.285^\circ$).

capacity. Therefore, the WF algorithm needs to be used when the Tx and Rx know the CSI.

V. CONCLUSIONS

In this paper, we have proposed a novel 6G STF non-stationary massive MIMO channel model jointly considering the MC, antenna efficiency, and near-field steering vectors. Also, a novel non-stationary channel capacity calculation method has been proposed. The influences

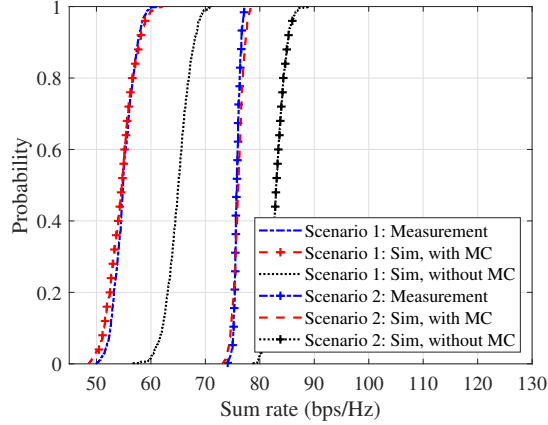


Fig. 15. Channel capacities of the non-stationary channel model with and without mutual coupling in comparison to the measurements when SNR=15 dB (Scenario 1: Outdoor, $N_t = 8, N_r = 128, f_c = 5.3$ GHz, $B = 160$ MHz. Scenario 2: Indoor, $N_t = 256, N_r = 16, f_c = 11$ GHz, $B = 200$ MHz).

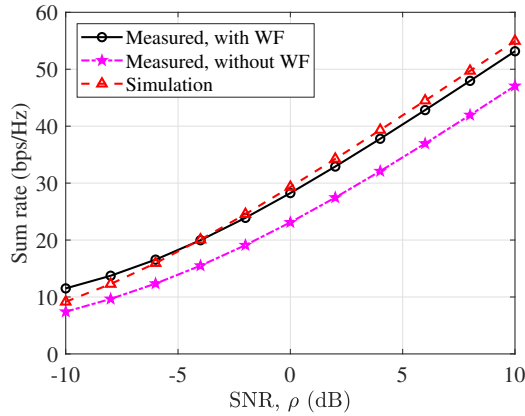


Fig. 16. Channel capacities of the non-stationary channel model with and without water-filling algorithm in comparison to the measurement ($N_t = 8, N_r = 128, f_c = 5.3$ GHz, $B = 160$ MHz, $\lambda_B = 40$ /m, $\lambda_D = 2$ /m, $v^{T(R)} = 0, \gamma = 10, \beta_A^T = 30^\circ, \beta_A^R = 0, \beta_E^T = 0,$ and $\beta_E^R = 70.285^\circ$).

of MC, antenna efficiency, and steering vectors on channel capacities have been analyzed and simulated. In comparison to the simulated spatial CCF without MC, the simulated one with MC is closer to the measurement results, which illustrates the necessity of considering MC in massive MIMO channels. The results have shown that different antenna topologies can influence channel capacities. UPA can achieve larger capacities than ULA and UCA when the antenna aperture is fixed. The non-stationary channel capacity is calculated as the summation of the channel capacities of separated WSS sub-channels. The channel capacity increases when the

number of WSS sub-channels increases within the spatial SI. The channel capacity which is calculated using the novel non-stationary channel capacity calculation method and considering MC matches the measurement results better in comparison to that using conventional calculation method and without MC. This illustrates the correctness of the non-stationary channel capacity calculation method and proves the improved accuracy of the proposed 6G non-stationary massive MIMO channel model considering the MC effect.

REFERENCES

- [1] C.-X. Wang, J. Huang, H. Wang, X. Gao, X.-H. You, and Y. Hao, "6G wireless channel measurements and models: Trends and challenges," *IEEE Veh. Technol. Mag.*, vol. 15, no. 4, pp. 22–32, Dec. 2020.
- [2] C.-X. Wang, X.-H. You, X. Gao, *et al.*, "On the road to 6G: Visions, requirements, key technologies and testbeds," *IEEE Commun. Surveys Tuts.*, vol. 25, no. 2, pp. 905–974, 2nd Quart., 2023.
- [3] M. D. Migliore, "On electromagnetics and information theory," *IEEE Trans. Antennas Propag.*, vol. 56, no. 10, pp. 3188–3200, Oct. 2008.
- [4] F. K. Gruber and E. A. Marengo, "New aspects of electromagnetic information theory for wireless and antenna systems," *IEEE Trans. Antennas Propag.*, vol. 56, no. 11, pp. 3470–3484, Nov. 2008.
- [5] R. Li, D. Li, J. Ma, *et al.*, "An electromagnetic-information-theory based model for efficient characterization of MIMO systems in complex space," *IEEE Trans. Antennas Propag.*, vol. 71, no. 4, pp. 3497–3508, Apr. 2023.
- [6] C. E. Shannon, "A mathematical theory of communication," *Bell Syst. Tech. J.*, vol. 27, no. 3, pp. 379–423, July 1948.
- [7] C. E. Shannon, "Communication in the presence of noise," *Proc. IRE.*, vol. 37, no. 1, pp. 10–21, Jan. 1949.
- [8] E. G. Larsson, O. Edfors, F. Tufvesson, and T. L. Marzetta, "Massive MIMO for next generation wireless systems," *IEEE Commun. Mag.*, vol. 52, no. 2, pp. 186–195, Feb. 2014.
- [9] J. G. Andrews, S. Buzzi, W. Choi, *et al.*, "What will 5G be?" *IEEE J. Sel. Areas Commun.*, vol. 32, no. 6, pp. 1065–1082, June 2014.
- [10] S. Wu, C.-X. Wang, and M. M. Alwakeel, "A general 3-D non-stationary 5G wireless channel model," *IEEE Trans. Commun.*, vol. 66, no. 7, pp. 3065–3078, July 2018.
- [11] J. Wang, C.-X. Wang, J. Huang, H. Wang, and X. Gao, "A general 3D space-time-frequency non-stationary THz channel model for 6G ultra massive MIMO wireless communication systems," *IEEE J. Sel. Areas Commun.*, vol. 39, no. 6, pp. 1576–1589, June 2021.
- [12] Y. Yuan, R. He, B. Ai, Z. Ma, Y. Miao, Y. Niu, *et al.*, "A 3D geometry-based THz channel model for 6G ultra massive MIMO systems," *IEEE Trans. Veh. Technol.*, vol. 71, no. 3, pp. 2251–2266, Mar. 2022.
- [13] Y. Yang, Y. Zheng, C.-X. Wang, and J. Huang, "Channel capacities of non-stationary 6G massive MIMO channels with mutual coupling verified by channel measurements," in *Proc. IEEE PIMRC'22*, Kyoto, Japan, Sept. 2022, pp. 1288–1293.
- [14] T. S. Rappaport, G. R. MacCartney, M. K. Samimi, and S. Sun, "Wideband millimeter-wave propagation measurements and channel models for future wireless communication system design," *IEEE Trans. Commun.*, vol. 63, no. 9, pp. 3029–3056, Sept. 2015.
- [15] M. El-Hadidy, T. O. Mohamed, F. Zheng, and T. Kaiser, "3D hybrid EM ray-tracing deterministic UWB channel model, simulations and measurements," in *Proc. IEEE ICUBW'08*, Hannover, Germany, Sept. 2008, vol. 2, pp. 1–4.
- [16] A. Hekkala, P. Kyösti, J. Dou, L. Tian, N. Zhang, W. Zhang, and B. Gao, "Map-based channel model for 5G wireless communications," in *Proc. 32nd URSI GASS*, Montreal, Canada, Aug. 2017, pp. 1–4.

- [17] J. Bian, C.-X. Wang, X. Gao, X. You, and M. Zhang, "A general 3D non-stationary wireless channel model for 5G and beyond," *IEEE Trans. Wireless Commun.*, vol. 20, no. 5, pp. 3211–3224, May 2021.
- [18] C.-X. Wang, Z. Lv, X. Gao, X.-H. You, Y. Hao, and H. Haas, "Pervasive channel modeling theory and applications to 6G GBSMs for all frequency bands and all scenarios," *IEEE Trans. Veh. Technol.*, vol. 71, no. 9, pp. 9159–9173, Sept. 2022.
- [19] J. Huang, C.-X. Wang, H. Chang, J. Sun, and X. Gao, "Multi-frequency multi-scenario millimeter wave MIMO channel measurements and modeling for B5G wireless communication systems," *IEEE J. Sel. Areas Commun.*, vol. 39, no. 9, pp. 2010–2025, Sept. 2020.
- [20] C. A. Balanis, *Antenna Theory: Analysis and Design*: Wiley, 1997.
- [21] J. W. Wallace and M. A. Jensen, "Mutual coupling in MIMO wireless systems: A rigorous network theory analysis," *IEEE Trans. Wireless Commun.*, vol. 3, no. 4, pp. 1317–1325, July 2004.
- [22] H. King, "Mutual impedance of unequal length antennas in echelon," *IRE Trans. Antennas Propag.*, vol. 5, no. 3, pp. 306–313, July 1957.
- [23] M. T. Ivrlač and J. A. Nossek, "Toward a circuit theory of communication," *IEEE Trans. Circuits Syst. I, Reg. Papers*, vol. 57, no. 7, pp. 1663–1683, July 2010.
- [24] T. Laas, J. A. Nossek, S. Bazzi, and W. Xu, "On reciprocity in physically consistent TDD systems with coupled antennas," *IEEE Trans. Wireless Commun.*, vol. 19, no. 10, pp. 6440–6453, Oct. 2020.
- [25] J. Gao, C.-X. Wang, J. Huang, and Y. Yang, "A novel circuit-based MIMO channel model considering antenna size and mutual coupling," in *Proc. WCSP'21*, Changsha, China, Oct. 2021, pp. 1–5.
- [26] M. Gustafsson, J. Aulin, M. Högberg, M. Alm, and B. Sahlbom, "Impact of mutual coupling on capacity in large MIMO antenna arrays," in *Proc. EuCAP'14*, Hague, Netherlands, Apr. 2014, pp. 2723–2727.
- [27] S. Saab, A. Mezghani, and R. W. Heath, "Optimizing the mutual information of frequency-selective multi-port antenna arrays in the presence of mutual coupling," *IEEE Trans. Commun.*, vol. 70, no. 3, pp. 2072–2084, Mar. 2022.
- [28] X. Chen, S. Zhang, and Q. Li, "A review of mutual coupling in MIMO systems," *IEEE Access*, vol. 6, pp. 24706–24719, Apr. 2018.
- [29] P. Ioannides and C. A. Balanis, "Uniform circular and rectangular arrays for adaptive beamforming applications," *IEEE Antennas Wireless Propag. Lett.*, vol. 4, pp. 351–354, 2005.
- [30] Z. Xiao, L. Zhu, Y. Liu, P. Yi, R. Zhang, X.-G. Xia, and R. Schober, "A survey on millimeter-wave beamforming enabled UAV communications and networking," *IEEE Commun. Surveys Tuts.*, vol. 24, no. 1, pp. 557–610, 1st Quart., 2022.
- [31] J. Liu and J. Li, "Robust detection in MIMO radar with steering vector mismatches," , vol. 67, no. 20, pp. 5270–5280, Oct. 2019.
- [32] T. Laas, J. A. Nossek, and W. Xu, "Limits of transmit and receive array gain in massive MIMO," in *Proc. WCNC'20*, Seoul, Korea, May 2020, pp. 1–8.
- [33] W. Tan and S. Ma, "Antenna array topologies for mmWave massive MIMO systems: Spectral efficiency analysis," *IEEE Trans. Veh. Technol.*, vol. 71, no. 12, pp. 12901–12915, Dec. 2022.
- [34] E. Telatar, "Capacity of multi-antenna Gaussian channels," *Eur. Trans. Telecommun.*, vol. 10, no. 6, pp. 585–595, Nov. 1999.
- [35] H. Shin and J. H. Lee, "Capacity of multiple-antenna fading channels: Spatial fading correlation, double scattering, and keyhole," *IEEE Trans. Inf. Theory*, vol. 49, no. 10, pp. 2636–2647, Oct. 2003.
- [36] S. Zhang and R. Zhang, "Capacity characterization for intelligent reflecting surface aided MIMO communication," *IEEE J. Sel. Areas Commun.*, vol. 38, no. 8, pp. 1823–1838, Aug. 2020.
- [37] X. Li, S. Zhou, E. Bjornson, and J. Wang, "Capacity analysis for spatially non-wide sense stationary uplink massive MIMO systems," *IEEE Trans. Wireless Commun.*, vol. 14, no. 12, pp. 7044–7056, Dec. 2015.

- [38] G. G. Raleigh and J. M. Cioffi, "Spatio-temporal coding for wireless communication," *IEEE Trans. Commun.*, vol. 46, no. 3, pp. 357–366, Mar. 1998.
- [39] 3GPP, "Study on channel model for frequencies from 0.5 to 100 GHz (Release 17)," TR 38.901, V17.0.0, Mar. 2022.
- [40] mmMAGIC, (May 2017). Measurement results and final mmMAGIC channel models, H2020-CT-671650-mmMAGIC/D2.2, v1.0. [Online]. Available: <https://5g-mmmagic.eu/results/>.
- [41] F. Alsaleem, J. S. Thompson, D. I. Laurenson, S. K. Podilchak, and C. A. Alistarh, "Small-size blockage measurements and modelling for mmWave communications systems," in *Proc. IEEE PIMRC'20*, London, UK., Aug. 2020, pp. 1–6.
- [42] G. L. Stüber, *Principles of Mobile Communications*, 2nd ed. Norwell, MA, USA: Kluwer, 2011.
- [43] X. Li and Z.-P. Nie, "Mutual coupling effects on the performance of MIMO wireless channels," *IEEE Antennas Wireless Propag. Lett.*, vol. 3, pp. 344–347, 2004.
- [44] G. H. Brown, "Directional antennas," *Proc. IRE.*, vol. 25, no. 1, pp. 78–145, Jan. 1937.
- [45] P.-S. Kildal, A. Vosoogh, and S. Maci, "Fundamental directivity limitations of dense array antennas: A numerical study using Hannan's embedded element efficiency," *IEEE Antennas Wireless Propag. Lett.*, vol. 15, pp. 766–769, 2016.
- [46] Y. Fei, Y. Fan, B. K. Lau, and J. S. Thompson, "Optimal single-port matching impedance for capacity maximization in compact MIMO arrays," *IEEE Trans. Antennas Propag.*, vol. 56, no. 11, pp. 3566–3575, Nov. 2008.
- [47] A. Paulraj, R. Nabar, and D. Gore, *Introduction to Space-Time Wireless Communications*, Cambridge: Cambridge University Press, 2008.
- [48] B. H. Fleury, M. Tschudin, R. Heddergott, D. Dahlhaus, and K. Ingeman Pedersen, "Channel parameter estimation in mobile radio environments using the SAGE algorithm," *IEEE J. Sel. Areas Commun.*, vol. 17, no. 3, pp. 434–450, Mar. 1999.
- [49] J. Li, B. Ai, R. He, M. Yang, Z. Zhong, and Y. Hao, "A cluster-based channel model for massive MIMO communications in indoor hotspot scenarios," *IEEE Trans. Wireless Commun.*, vol. 18, no. 8, pp. 3856–3870, Aug. 2019.

Response to the Reviewers' Comments on 1570895543:

“Characteristics and Channel Capacity Studies of a Novel 6G Non-Stationary Massive MIMO Channel Model Considering Mutual Coupling”

The authors would like to thank the editor and all the reviewers for their helpful and insightful comments. We have improved the quality of the manuscript by carefully taking all the comments into account. The modifications in this revised manuscript as well as the response to the reviewers' comments are described below.

Editor's comments

While reviewers appreciate the technical depth, they raise several concerns about the novelty of the approach (particularly in contrast to your previously published work on channel modelling) and the underlying technical assumptions. Thus, we invite you to further revise your work to address the reviewer's comments and resubmit the revised manuscript for further evaluation.

Response: We have tried our best to further improve the quality of the manuscript by carefully addressing the editor's and all the reviewers' concerns. The detailed point-to-point response to the reviewers' comments is provided below.

Reviewer: 1

Detailed Comments

1. First of all I find the idea that new channel models are needed with mutual coupling a bit imprecise, because one can actually separate the channel modeling for the propagation channel and the effects of mutual coupling, which together lead to the channel between the ports of the transmitting and receiving antenna arrays - at least as long as they are not in each other's reactive near field. You can also see this in (1).

Response: With some key 6G technologies such as holographic MIMO, the antenna spacing can decrease as the number of antenna elements increases within a limited aperture. When the antenna spacing is reduced, the mutual coupling will have a significant influence on the antenna parameters such as antenna pattern and will affect the statistical properties of wireless propagation channels. In such cases, it is necessary to jointly model the propagation channel and the mutual coupling effect. Furthermore, 6G wireless communications tend to work at higher frequency bands. The wavelength will be smaller and the Rayleigh distance will be larger. The far-field assumption is not easy to be fulfilled and the near-field spherical wavefront has to be considered. Additionally, the antenna patterns affected by mutual coupling are presented in (1), which shows that the mutual coupling cannot be separated from channels.

2. To be honest, I found it difficult to understand what exactly the contribution is. It is claimed that one of the main contributions is that the novel channel model that is introduced also takes antenna efficiency into account, where supposedly the definition comes from [37], but it does not appear there. So where does the definition in (47) come from? It appears to me that (47) is actually the

[same as the embedded element's maximum available total radiation efficiency as defined in \(2\) in P.-S. Kildal, A. Vosoogh, and S. Maci, "Fundamental Directivity Limitations of Dense Array Antennas: A Numerical Study Using Hannan's Embedded Element Efficiency," IEEE Antennas and Wireless Propagation Letters, vol. 15, 2016.](#)

[However, this paper was not cited, and there are restrictions on antenna spacing, etc. for the definition to hold, which are not mentioned in the paper under review.](#)

Response: Eq. (40) (Eq. (47) in the original manuscript) comes from the reference [45]. In the previous work, the widely used geometry-based statistical models (GBSMs) only considered the number of antenna elements, antenna size, and antenna pattern. They did not take the mutual coupling and antenna efficiency into consideration. In the current paper, we add the mutual coupling and antenna efficiency in the ultra-massive MIMO GBSM. As for the antenna efficiency, we define it under two conditions and cite the relevant reference [45]. In the revised manuscript, we have added the citation and restrictions of Eq. (40) (Eq. (47) in the original manuscript) in Section II-D (see sentences in the blue font on Page 14):

“When the element spacing is less than half-wavelength, the antenna efficiency of each element at the Rx can be calculated as [45]

$$\eta_q(\delta_q) = \frac{\pi L_{r,x} L_{r,y}}{N_r \lambda^2} = \frac{\pi \delta_q^2}{\lambda^2} \quad (40)$$

where $L_{r,x}$ and $L_{r,y}$ are the length and width of antenna array at the Rx side, respectively. In addition, the antenna efficiency for more complicated antenna arrays may need to use the full-wave simulation to obtain, which is given as

$$\eta_q = \frac{P_T - P_{q,loss}}{P_T} \quad (41)$$

where P_T is the transmit power and $P_{q,loss}$ is the return loss power of the q th port, which can be obtained in the full-wave simulation software.

[45] P.-S. Kildal, A. Vosoogh, and S. Maci, “Fundamental directivity limitations of dense array antennas: A numerical study using Hannan's embedded element efficiency,” *IEEE Antennas Wireless Propag. Lett.*, vol. 15, pp. 766 – 769, 2016.”

3. [Then I wonder whether it makes sense to use this formula when it is said at the same time that the load and antenna impedances are optimized according to \[53\]. Isn't this contradictory? In any case the idea that radiation efficiency and mutual coupling are separate is flawed, because radiation efficiency depends on self and mutual impedance, and load impedance.](#)

Response: In the mutual coupling matrix, self-impedance, mutual impedance, and load impedance need to be determined. Eqs. (34)-(39) are used to calculate the self-impedance and mutual impedance, and the load impedance is optimized by using the single-port matching method, which used the value of self-impedance and mutual impedance [46] ([53] in the original manuscript). Therefore, they are related and not contradictory. Additionally, when using the full-wave simulation method, the return loss in radiation efficiency is influenced by the self-impedance, mutual impedance, and load impedance in the mutual coupling matrix. Therefore, the antenna efficiency is included in the mutual coupling effect and they are not separated.

In order to explain the self-impedance and mutual impedance in more detail, in the revised manuscript we have added some descriptions in Section II-C (see sentences in the blue font on Pages 13 and 14):

“In (30), the mutual impedance matrix \mathbf{Z} is defined in [22] with different antenna topologies. The self-impedance is the diagonal element of \mathbf{Z} , while the non-diagonal element is the mutual impedance between different antenna elements. According to the reciprocity theorem, the mutual impedance between two antennas can be computed as

$$Z_{12} = Z_{21} = -\frac{i_1 i_2}{i_{1m} i_{2m}} \cdot \frac{v_2^0}{i_1} = -30 \left[\left(\int_h^{l_2+h} \sin \beta(z-h) + \int_{l_2+h}^{2l_2+h} \sin \beta(2l_2+h-z) \right) \left(\frac{-je^{-j\beta r_1}}{r_1} + \frac{-je^{-j\beta r_2}}{r_2} + \frac{2j \cos \beta l_1 e^{-j\beta r_0}}{r_0} \right) dz \right]. \quad (37)$$

“The self-impedance is defined as

$$Z_{11} = \left. \frac{V_1}{I_1} \right|_{I_2=0}, Z_{22} = \left. \frac{V_2}{I_2} \right|_{I_1=0} \quad (39)$$

where V_1 and V_2 are induced voltages generated by the currents I_1 and I_2 on antennas 1 and 2, respectively. Under this condition, Z_{11} and Z_{22} are the exact meanings of antenna input impedance. For the load impedance \mathbf{Z}_L , it is optimized for capacity maximization using the single-port matching method [46]. For other antenna arrangements, the impedance matrix can be obtained by utilizing electromagnetic calculation methods.

*[46] Y. Fei, Y. Fan, B. K. Lau, and J. S. Thompson, “Optimal single-port matching impedance for capacity maximization in compact MIMO arrays,” *IEEE Trans. Antennas Propag.*, vol. 56, no. 11, pp. 3566–3575, Nov. 2008.”*

4. [In general, I find the presentation unbalanced. There is too much information on some things, for example spending an entire page on part of the derivation of the formulas for the mutual impedance of parallel dipoles made from infinitely thin but perfectly conducting wires, but completely omitting self-impedance. There is too little information about the setup of the system for the comparison with simulation results. For example it is not clear to me whether all antenna arrays consist of dipoles.](#)

Response: In the revised manuscript, the derivation of the mutual impedance of dipoles has been described concisely and the calculation of self-impedance has been added to balance the presentation. In addition, the configurations of the antenna array have been added in Section IV-A (see sentences in the blue font on Page 21):

“There are 4 switch boxes at the Rx and they can receive 4 parallel signals. Each switch box is capable of receiving 32 serial signals, thus a total of 128 channels can be measured. The antenna on each channel is composed of 8 vertical omni-directional patch antennas, which are used for vertical beamforming.”

5. [If I understand the formulas in Section II-A correctly, the matrix \$\mathbf{H}_{SSF}\$ is actually the channel frequency response matrix instead of the channel impulse response matrix, because otherwise a convolution in \(1\) would be necessary instead of a multiplication.](#)

Response: In (1), the matrix H_{SSF} is the channel impulse response matrix, which is the multiplication of the small-scale fading and large-scale fading that is in the power scale. Channel impulse response is a function of time and delay, while channel frequency response is a function of frequency. They can be converted to each other by the Fourier or inverse Fourier transform.

6. [I don't understand the sentence "Notably, wireless channel originating from antennas and carrying information via electromagnetic waves, is beneficial for channel estimation, channel capacity analysis, and network planning \[2\].", because any wireless channel is based on how the electromagnetic waves propagate between the antennas.](#)

Response: This description is to explain the position and role of wireless channels in communication systems, as well as the relationship between wireless channels and electromagnetic theory, antenna theory, and information theory. That is the reason why we study the ultra-massive MIMO channel model to combine the electromagnetic theory and information theory. In the revised manuscript, we have modified the descriptions of the wireless channel in Section I (see sentences in the blue font on Page 2):

"The wireless propagation channel links the transmitter (Tx) and receiver (Rx) antennas and carries information via electromagnetic waves, acting as the bridge connecting electromagnetic theory and information theory. The wireless channel modeling theory is of great importance for channel estimation, channel capacity analysis, and network planning."

7. [Some of the authors had a conference paper at PIMRC 2022 \(see reference 19\), which is very similar to this paper, but the manuscript does not state clearly how they are related. What exactly is the additional contribution?](#)

Response: The PIMRC'22 conference paper [13] ([19] in the original manuscript) proposed a non-stationary massive MIMO channel model and analyzed the statistical properties in the space domain as well as channel capacities. However, it did not consider the antenna efficiency and near-field steering vectors, and the analysis of statistical properties and channel capacities was limited. In the revised manuscript, we have added the difference between the conference paper and this paper in Section I (see sentences in the blue font on Page 4):

"This paper further extends our previous work in [13] to fill the research gaps. Specifically, [13] only considered the MC effect in a non-stationary massive MIMO channel model and analyzed the spatial cross-correlation function (CCF) as well as channel capacities. In this paper, the proposed novel 6G STF non-stationary massive MIMO channel model jointly considers antenna MC effect, antenna efficiency, and near-field steering vectors."

8. [I recommend to remove the claim that you propose a novel non-stationary channel capacity calculation method for non-stationary channels, because the idea of dividing the channel into WSS sub-channels is hardly new.](#)

Response: Although the idea of dividing the non-stationary channel into WSS sub-channels is not new, the idea of using this method in calculating non-stationary channel capacities is first proposed in this paper. Most importantly, the method of calculating non-stationary channel capacities without

dividing the non-stationary channel into WSS sub-channels is not correct. Hence, we would like to keep the claim in the revised manuscript.

9. [Their authors reference too many of their own papers \(20 out of 55 references if I am not mistaken\).](#)

Response: In the revised manuscript, we have deleted some of our papers as suggested and added some new relevant references.

Reviewer: 2

[Detailed Comments](#)

1. [Is it possible to include more descriptions in the figure titles?](#)

Response: In the revised manuscript, we have included more descriptions in the figure titles (see titles of Figs. 4, 6, 8-12, 15 and 16).

“Fig. 4. The illustrations of steering vectors for (a) uniform linear array, (b) uniform plane array, and (c) uniform circular array.

Fig. 6. (a) Real measurement environment and (b) sketch map of the outdoor ultra-massive MIMO scenario.

Fig. 8. (a) Spatial cross-correlation function at different antenna elements, (b) Temporal autocorrelation function at different time instants, and (c) Frequency correlation function at different carrier frequencies of the non-stationary channel model ($N_t=8$, $N_r=1024$, $\lambda_B=40/m$, $\lambda_D=2/m$, $v^{T(R)}=10$ m/s, and $\gamma=30$).

Fig. 9. Normalized coherence distances of the non-stationary channel model with different elevation angles of the Rx array.

Fig. 10. Simulated and measured Doppler power spectral densities of the non-stationary channel model with different elevation angles of the Rx array.

Fig. 11. Analytical, simulated, and measured spatial cross-correlation functions with and without mutual coupling ($f_c=5.3$ GHz, $B=160$ MHz, $v^{T(R)}=0$, $D=58$ m, $\beta_A^T=30^\circ$, $\beta_E^T=0$, $\beta_A^R=0$, and $\beta_E^R=70.285^\circ$).

Fig. 12. Measured angular power spectral densities and fitted Laplace distributions of (a) Tx1, (b) Tx2, and (c) Tx3 ($f_c=5.3$ GHz, $B=160$ MHz, $v^{T(R)}=0$, $D=58$ m, $\beta_A^T=30^\circ$, $\beta_E^T=0$, $\beta_A^R=0$, and $\beta_E^R=70.285^\circ$).

Fig. 15. Channel capacities of the non-stationary channel model with and without mutual coupling in comparison to the measurements when SNR=15 dB (Scenario 1: Outdoor, $N_t=8$, $N_r=128$, $f_c=5.3$ GHz, $B=160$ MHz. Scenario 2: Indoor, $N_t=256$, $N_r=16$, $f_c=11$ GHz, $B=200$ MHz).

Fig. 16. Channel capacities of the non-stationary channel model with and without water-filling algorithm in comparison to the measurement ($N_t = 8$, $N_r = 128$, $f_c = 5.3$ GHz, $B = 160$ MHz, $\lambda_B = 40/m$, $\lambda_D = 2/m$, $v^{T(R)} = 0$, $\gamma = 10$, $\beta_A^T = 30^\circ$, $\beta_E^T = 0$, $\beta_A^R = 0$, and $\beta_E^R = 70.285^\circ$).

2. [Please include the axis for Fig.2 and try to re-organize Fig.1 so that it looks clearer. In fig.8 a,b,c please make the legend a bit clearer.](#)

Response: In the revised manuscript, we have included the axis for Fig. 2 and reorganized Fig. 1 to make it look clearer. In Fig. 8, the analytical result was obtained through the plot of the theoretical derivation result of the space-time-frequency correlation functions according to Eq. (53), while the simulation result was obtained by simulating the correlation functions of the channel starting from the impulse response. The analytical result fits the simulation result very well, illustrating the correctness of both derivations and simulations. In the revised manuscript, we have added explanations of the analytical results and simulation results in Section IV-B (see sentences in the blue font on Page 22):

“The analytical results were obtained through the plot of the theoretical derivation results of the STF correlation functions according to (53), while the simulation results were obtained by simulating the correlation functions of the channel starting from the impulse response.”

3. [In the measured results, why were the values of the \$N_t\$ and \$N_r\$ chosen this way? Is there a significance for a desired throughput? Also, the frequency and bandwidth seem to be a bit low for 6G especially when near field is being considered. I am wondering if any study was made on higher frequencies with larger BWs?](#)

Response: The values of N_t and N_r are decided by the capabilities of the channel sounder and we set these values according to the channel measurement setups. In the literature, there are some massive MIMO channel measurements with higher frequencies and larger bandwidths in 6G communication systems. In [49], the channel measurements of an indoor scenario were carried out on 11 GHz with 200 MHz bandwidth. In the revised manuscript, we have added the comparative validation with the measurements in [49].

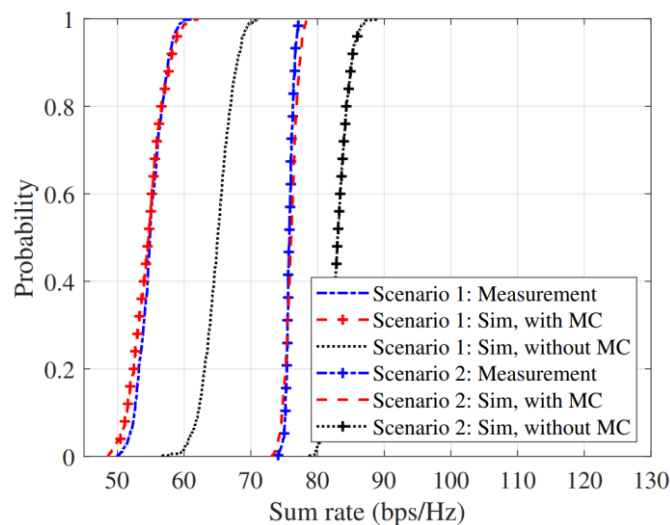


Fig. 15. Channel capacities of the non-stationary channel model with and without mutual coupling in comparison to the measurements when SNR=15 dB (Scenario 1: Outdoor, $N_t=8$, $N_r=128$, $f_c=5.3$ GHz, $B=160$ MHz. Scenario 2: Indoor, $N_t=256$, $N_r=16$, $f_c=11$ GHz, $B=200$ MHz).

[49] J. Li, B. Ai, R. He, M. Yang, Z. Zhong, and Y. Hao, "A cluster-based channel model for massive MIMO communications in indoor hotspot scenarios," *IEEE Trans. Wireless Commun.*, vol. 18, no. 8, pp. 3856–3870, Aug. 2019.

4. [The effect of MC seems to be detrimental but if proper matching was done for the UPA I think you can use MC to your benefit \(you can emphasize this point by referring to ref \[36\]\).](#)

Response: When using the proper matching for specific antenna arrays, the mutual coupling effect can be declined and the communication system may achieve a better performance. In the revised manuscript, we have added the description of the proper matching on system performance by referring to [27] ([36] of the previous manuscript) in Section I (see sentences in blue font on Page 3):

"This work also claimed that the performance degradation due to MC effect can be declined by adopting a proper matching method for wideband antennas and can achieve the maximum achievable rate."

5. [It will be nice to have a set of scenarios to proof that the new non-stationary channel capacity calculation method holds. Having one scenario might show that it works here but not for others.](#)

Response: In the revised manuscript, we have added the indoor channel measurements on a higher frequency in Fig. 15. After the comparison with the measurement, it is found that the simulation results of the channel capacity are in good agreement with the measurement results, which proves the correctness of the new non-stationary channel capacity calculation method. The description of channel measurements and corresponding analysis are described in Section IV-C (see sentences in the blue font on Page 26):

"Scenario 1 is the outdoor ultra-massive MIMO with Tx2 and Rx in Fig. 6(a), and scenario 2 is the indoor theater channel measured in [49]."

[49] J. Li, B. Ai, R. He, M. Yang, Z. Zhong, and Y. Hao, "A cluster-based channel model for massive MIMO communications in indoor hotspot scenarios," *IEEE Trans. Wireless Commun.*, vol. 18, no. 8, pp. 3856–3870, Aug. 2019."

Reviewer: 3

[Detailed Comments](#)

[The paper considers the joint impact of mutual coupling, near-field effects, and space-time-frequency non-stationarity of the massive MIMO channels. The accuracy of the proposed channel modeling is verified by real channel measurements. However, most of the equations are taken from previous works such as \[24\], \[31\], \[52\]. The novelty and the challenges of the joint consideration of mutual coupling, near-field effects, and space-time-frequency non-stationarity are not clearly explained. Please see my additional comments:](#)

1. [I think there is something wrong with Eqn. \(2\). Why is only one value of "n" and "m" considered?](#)

Response: In the revised manuscript, we have checked and revised the channel impulse response of the proposed channel model in Eq. (2), and it is corrected as

$$h_{qp,fc}(t, \tau) = \sqrt{\frac{K_R(t)}{K_R(t)+1}} h_{qp,fc}^{\text{LoS}}(t, \tau) + \sqrt{\frac{1}{K_R(t)+1}} h_{qp,fc}^{\text{NLoS}}(t, \tau) \quad (2)$$

The corresponding LoS component can be updated as

$$h_{qp,fc}^{\text{LoS}}(t, \tau) = \begin{bmatrix} F_{q,H}(\theta_L^R, \phi_L^R) \\ F_{q,V}(\theta_L^R, \phi_L^R) \end{bmatrix}^T \begin{bmatrix} e^{j\Phi_L^{\theta\theta}} & 0 \\ 0 & e^{j\Phi_L^{\phi\phi}} \end{bmatrix} \begin{bmatrix} F_{p,H}(\theta_L^T, \phi_L^T) \\ F_{p,V}(\theta_L^T, \phi_L^T) \end{bmatrix} \cdot \left(\frac{f}{f_c}\right)^{\gamma_L} \cdot e^{-j\frac{2\pi}{\lambda}d_{2D}} \cdot e^{j2\pi f_c \tau_{qp}^L(t)} \cdot \delta(\tau - \tau_{qp}^L(t)) \quad (3)$$

and the NLoS components can be expressed as

$$h_{qp,fc}^{\text{NLoS}}(t, \tau) = \sum_{n=1}^{N(t)} \sum_{m=1}^{M(t)} \begin{bmatrix} F_{q,H}(\theta_{n,m}^R, \phi_{n,m}^R) \\ F_{q,V}(\theta_{n,m}^R, \phi_{n,m}^R) \end{bmatrix}^T \begin{bmatrix} e^{j\Phi_{n,m}^{\theta\theta}} & \frac{e^{j\Phi_{n,m}^{\theta\phi}}}{\sqrt{\kappa_{n,m}}} \\ \frac{e^{j\Phi_{n,m}^{\phi\theta}}}{\sqrt{\kappa_{n,m}}} & e^{j\Phi_{n,m}^{\phi\phi}} \end{bmatrix} \begin{bmatrix} F_{p,H}(\theta_{n,m}^T, \phi_{n,m}^T) \\ F_{p,V}(\theta_{n,m}^T, \phi_{n,m}^T) \end{bmatrix} \cdot \sqrt{P_{qp,n,m}(t)} \cdot \left(\frac{f}{f_c}\right)^{\gamma_{n,m}} \cdot \mathbf{\Omega}_{q,n,m}^T \cdot e^{j2\pi f_c \tau_{qp,n,m}(t)} \cdot \delta(\tau - \tau_{qp,n,m}(t)) \cdot \mathbf{\Omega}_{p,n,m} \quad (9)$$

2. [It seems that \$d_{2D}\$ is not defined in Eqn. \(3\). Moreover, the frequency-dependent term and the physical interpretation of the parameter \$\gamma_L\$ should be explained. In addition, what is the mathematical form and dimension of steering vectors that correspond to only a single antenna in Eqn. \(3\)?](#)

Response: The dimension of steering vectors of a single antenna is one. Therefore, the steering vector in LoS component channel impulse response can be omitted. In the revised manuscript, we have modified the expression of Eq. (3) and added the meaning of d_{2D} and γ_L in Section II-A (see sentences in the blue font on Page 6):

$$h_{qp,fc}^{\text{LoS}}(t, \tau) = \begin{bmatrix} F_{q,H}(\theta_L^R, \phi_L^R) \\ F_{q,V}(\theta_L^R, \phi_L^R) \end{bmatrix}^T \begin{bmatrix} e^{j\Phi_L^{\theta\theta}} & 0 \\ 0 & e^{j\Phi_L^{\phi\phi}} \end{bmatrix} \begin{bmatrix} F_{p,H}(\theta_L^T, \phi_L^T) \\ F_{p,V}(\theta_L^T, \phi_L^T) \end{bmatrix} \cdot \left(\frac{f}{f_c}\right)^{\gamma_L} \cdot e^{-j\frac{2\pi}{\lambda}d_{2D}} \cdot e^{j2\pi f_c \tau_{qp}^L(t)} \cdot \delta(\tau - \tau_{qp}^L(t)) \quad (3)$$

“The parameter γ_L is a scenario-dependent value in the LoS path, and it describes the trend of how amplitude decreases as frequency increases. The projection of the transceiver distance on the ground is denoted as d_{2D} .”

3. [Why is there no elevation velocity component in the last line of Eqn. \(8\)? Moreover, is there a need to introduce a new notation, i.e., \$\alpha^R\$, in addition to the notation in Eqn. \(7\) for the velocity direction?](#)

Response: The elevation velocity component needs to be considered in the last line of Eq. (8). In the revised manuscript, we have modified Eq. (8) and defined the notations of α^R and α^T in Eq. (8) in Section II-A (see sentences in the blue font on Page 8):

“When the Tx and Rx are traveling with constant velocity, $D_{qp}(t)$ in (5) can be calculated as

$$\begin{aligned}
D_{qp}(t)^2 = & \left[\cos(\alpha^R)v^R t - \cos(\alpha^T)v^T t - \cos(\beta_E^T)\cos(\beta_A^T)\delta_p + \cos(\beta_E^R)\cos(\beta_A^R)\delta_q \right]^2 \\
& + \left[\sin(\alpha^R)v^R t - \sin(\alpha^T)v^T t - \cos(\beta_E^T)\sin(\beta_A^T)\delta_p + \cos(\beta_E^R)\cos(\beta_A^R)\delta_q \right]^2 \quad (8) \\
& + \left[\sin(\beta_E^T)\delta_p - \sin(\beta_E^R)\delta_q + \sin(\theta_v^R)v^R t - \sin(\theta_v^T)v^T t \right]^2
\end{aligned}$$

where $\cos(\alpha^R) = \cos(\theta_v^R)\cos(\phi_v^R)$ and $\sin(\alpha^R) = \cos(\theta_v^R)\sin(\phi_v^R)$, and the corresponding $\cos(\alpha^T)$ and $\sin(\alpha^T)$ can be obtained by substituting the superscript R with T .

4. [Why are the antenna spacings at the Tx and Rx so specific numbers such as 0.88 and 0.6 \$\lambda\$? Why are they greater than half-a-wavelength spacing?](#)

Response: In general, the antenna spacing is usually half-wavelength in antenna analysis. However, in the actual production of antenna arrays, the antenna spacing will be slightly greater than half-wavelength due to the isolation between antenna elements and the size requirements of each antenna element. The utilized antenna array is manufactured by a commercial company, so the antenna spacing is fixed in the channel measurements.

5. [How is the capacity measured in a real channel environment without knowing the coding and modulation that achieves it?](#)

Response: The channel capacity is calculated based on the measured channel matrix according to the proposed non-stationary channel capacity calculation method in (71). The channel measurement system directly transmit and receive signals without coding and modulation. Hence, the coding and modulation schemes are not considered in the channel capacity calculation.

6. [My main concern is that the paper seems just a combination of previously developed equations in the works \[24\], \[31\], \[52\]. The added novelty and challenges are not clear.](#)

Response: This paper is not just a combination of previously developed equations in the works [17], [22], [43] ([24], [31], [52] in the original manuscript). In [17], the authors ignored the mutual coupling effect and near-field steering vectors in the massive MIMO channel model. In [22], the mutual impedance of dipole antennas was derived. However, it did not consider the antenna efficiency and calculate the self-impedance and mutual impedance of other types of antenna array. In [43], the mutual coupling effect was considered in the spatial correlation model. However, this channel model did not include space-time-frequency non-stationarity and near-field spherical wavefront effect. In our paper, a novel 6G space-time-frequency non-stationary massive MIMO geometry-based statistical model is proposed, which jointly considers the mutual coupling, near-field steering, and antenna efficiency. These novelties are clearly mentioned in the original manuscript (see sentences at the end of Section I on Page 4).